

A UNIFIED APPROACH TO MOTION CONTROL OF MOBILE ROBOTS

Hamayoun Seraji

Jet Propulsion Laboratory
California Institute of Technology
Pasadena, CA 91109

Abstract

This paper presents a simple on-line approach for motion control of mobile robots comprised of a manipulator arm mounted on a mobile base. The proposed approach is equally applicable to non-holonomic mobile robots such as rover-mounted manipulators and to holonomic mobile robots such as tracked robots or compound manipulators. For wheeled mobile robots, the non-holonomic base constraints are incorporated directly into the task formulation as kinematic constraints. The configuration control approach is utilized to exploit the redundancy introduced by the base mobility in order to perform a set of user-specified additional tasks during the end-effector motion, while satisfying the non-holonomic base constraints (if applicable). This framework allows the user to assign weighting factors to individual base and arm configuration parameters, as well as to each task specification. The computational efficiency of the proposed control scheme makes it particularly suitable for real-time implementation. Two simulation studies are discussed to demonstrate the application of the motion control scheme to a rover-mounted arm (non-holonomic system) and to a tracked robot (holonomic system). An experimental study is also presented on motion control of a Robotics Research arm mounted on a tracked mobile platform at JPL.

1 Introduction

Robot manipulators mounted on mobile platforms will be utilized increasingly in both terrestrial and space applications. For instance, NASA is planning to use a tracked compound manipulator arm for the Space Station Freedom, and to utilize manipulator arms mounted on Mars-rovers for Marsexploration. In mobile robots, the base mobility increases the size of the robot workspace substantially, and enables proper positioning of the manipulator for efficient task execution. Typical examples of mobile robots are tracked robots, gantry robots, compound robots, and wheeled robots.

In recent years, path planning and motion control of mobile robots have been active areas of research [see, e.g., 1-13]. When the base mobility is provided by a track, a gantry, or another robot, the kinematics of the base platform has *holonomic constraints* similar to the kinematics of the manipulator itself; thus the base can effectively be treated as additional revolute or prismatic joints of the manipulator. On the other hand, wheeled mobile platforms are subject to non-integrable kinematic constraints, known as *non-holonomic constraints*. Such constraints are generally caused by one or several rolling contacts between rigid bodies, and reflect the fact that the wheeled platform must move in the direction of its main axis of symmetry. A rover is a typical non-holonomic mechanical system. It can attain any position in the plane of motion with any orientation; hence the configuration space is three-dimensional. However, the velocity of motion must always satisfy a non-holonomic constraint; thus the space of achievable velocities is two dimensional.

In recent years, there has been a growing interest in the analysis and control of both holonomic and non-holonomic mobile robots. Carricker, Khosla, and Krogh [1-2] formulate the coordination of mobility and manipulation as a nonlinear optimization problem. A general cost function for point-to-point motion in Cartesian space is defined and is minimized using a simulated annealing method. Pin and Culoli [3-4] define a weighted multi-criteria cost function which is then optimized using Newton's algorithm. Hootsmans and Dubowsky [5] (1cve1o) an extended Jacobian transpose control method to compensate for dynamic interactions between the manipulator and the base. Seraji [6] describes a simple on-line method for motion control of holonomic mobile robots. For non-holonomic mobile robots, path planning and motion control have attracted considerable research in recent years [7-13]. In a classic paper [7], Barraquand and Latombe derive the non-holonomic rover constraint and discuss optimal maneuvering of mobile robots. Yamamoto and Yun [8-9] address coordination of locomotion and manipulation and solve the problem of following a moving surface. Wang and Kumar [10-11] associate compliance functions to the mobile manipulator joints and implement rate decomposition using screw theory. Liu and Lewis [12-13] develop a decentralized robust controller for trajectory tracking of the mobile manipulator end-effector.

In this paper, the configuration control methodology developed earlier [14-15] for redundant robot control is utilized for motion control of both holonomic and non-holonomic mobile robots. The non-holonomic kinematic constraints for wheeled robots fit naturally in the configuration control formulation. The non-holonomic kinematic constraint, the desired

end-effector motion, and the user-specified redundancy resolution goals are combined to form a set of augmented tasks. These tasks are then accomplished using the configuration control approach to determine the motion of each mobility and manipulation degree-of-freedom.

This paper is structured as follows. In Section 2, motion control of non-holonomic mobile robots is formulated and solved using the configuration control approach, and a simulation study of a rover-mounted arm is presented for illustration. For holonomic mobile robots, the motion control scheme is discussed in Section 3, and is illustrated by application to a tracked robot. Section 4 presents an experimental study of the proposed motion control scheme applied to a Robotics Research arm mounted on a track at JPL. Section 5 discusses the results of the paper and draws some conclusions.

2 Motion Control of Mobile Robots with Non-Holonomic Base Constraint(s)

In this section, we consider a mobile robot comprised of a manipulator arm mounted on a mobile base with a non-holonomic constraint. The most common example of such system is a rover-mounted manipulator that will be studied in detail in this section.

We first develop a simple kinematic model that represents the rover-plus-manipulator system, and then describe a motion control scheme for this system. We propose a fully *integrated* kinematic representation and motion control scheme for the rover and the manipulator, rather than treating the rover and the manipulator as two separate entities. From this view, the integrated system is composed of two closely interacting subsystems with different kinematic and dynamic characteristics. The rover subsystem, being a wheeled vehicle, is subject to non-holonomic constraints; whereas for the manipulator subsystem, the constraints are holonomic.

The kinematics of the rover and the manipulator subsystems are studied in Sections 2.1 and 2.2, followed by the motion control scheme in Section 2.3.

2.1 Non-holonomic Rover Subsystem

Consider a front-wheel-drive four-wheel rover. The rover is represented by a two-dimensional rectangular object translating and rotating in the plane of motion, as illustrated in Figure 1. Let $F(x_f, y_f)$ denote the midpoint between the two front wheels and $R(x_r, y_r)$ represent the midpoint between the two rear wheels of the rover, where the coordinates are expressed with respect to the fixed world frame $\{W\}$ with axes $(0x, 0y)$ shown in Figure 1. The rover configuration is parameterized by the 3×1 vector $p = [x_f, y_f, \phi]^T$, where ϕ denotes the orientation of the main axis of the rover relative to the x -axis of the world frame.

Assuming a pure rolling contact between the rover wheels and the ground, i.e., no slipping, the velocity of point R is always along the main axis of the rover. Hence, we

have

$$\dot{x}_r = \lambda \cos \phi ; \quad \dot{y}_r = \lambda \sin \phi \quad (1)$$

where λ is a scalar. Eliminating λ , we obtain

$$\dot{x}_r \sin \phi - \dot{y}_r \cos \phi = 0 \quad (2)$$

Equation (2) can be expressed in terms of the coordinates (x_f, y_f) of the front point F on the FOF('r). The coordinates of the rear point $R(x_r, y_r)$ and the front point $F(x_f, y_f)$ are related by

$$x_f = x_r + l \cos \phi ; \quad y_f = y_r + l \sin \phi \quad (3)$$

where l denotes the distance between R and F , i.e., the rover length. Thus, the velocities of R and F are related by

$$\dot{x}_f = \dot{x}_r + l \dot{\phi} \sin \phi ; \quad \dot{y}_f = \dot{y}_r + l \dot{\phi} \cos \phi \quad (4)$$

From equations (2) and (4), we obtain the following *non-holonomic kinematic constraint*

$$\dot{x}_f \sin \phi - \dot{y}_f \cos \phi + \dot{\phi} l = 0 \quad (5)$$

or, in matrix form

$$[\sin \phi \quad -\cos \phi \quad l] \dot{p} = 0 \quad (6)$$

where $\dot{p} = [\dot{x}_f, \dot{y}_f, \dot{\phi}]^T$. Equation (6) represents a natural constraint that must be satisfied by the velocity vector \dot{p} , [7]. It is seen that at any configuration (x_f, y_f, ϕ) , the space of velocities $(\dot{x}_f, \dot{y}_f, \dot{\phi})$ achievable by the rover is restricted to a two-dimensional subspace in view of the constraint (6). This implies that the velocity vector \dot{p} is completely determined by the configuration vector p and, say, \dot{x}_f and \dot{y}_f . Notice that the achievable configuration space (x_f, y_f, ϕ) of the rover is three-dimensional, i.e., is completely unrestricted. Note that equation (6) is a special form of the non-holonomic constraint

$$G(p)\dot{p} = 0 \quad (7)$$

where G is an $m \times n$ matrix and p is the $n \times 1$ vector of generalized coordinates of the system. A kinematic constraint of the form (7) is called non-holonomic if it is non-integrable; i.e., \dot{q} can not be eliminated and the constraint (7) can not be rewritten in terms of q alone in the form $H(q) = 0$. Otherwise, the constraint is called holonomic.

Now, the control variables of the rover are the velocity v of the front wheels and the steering angle γ between the front wheels and the main axis of the rover. Therefore, the velocity variables are related to the control variables by

$$\begin{aligned} \dot{x}_f &= v \cos(\phi + \gamma) \\ \dot{y}_f &= v \sin(\phi + \gamma) \\ \dot{\phi} &= \frac{v}{l} \sin \gamma \end{aligned} \quad (8)$$

where the third equation is derived from the first two and the constraint (6). Given $(\dot{x}_f, \dot{y}_f, \dot{\phi})$, the rover velocity v and the steering angle γ are found from equation (8) as

$$v = [\dot{x}_f^2 + \dot{y}_f^2]^{\frac{1}{2}} ; \quad \gamma = \sin^{-1} \left[\frac{\dot{\phi}l}{(\dot{x}_f^2 + \dot{y}_f^2)^{\frac{1}{2}}} \right] \quad (9)$$

2.2 1 Iolonomic Manipulator Subsystem

For simplicity of presentation, we consider a planar two-link manipulator arm mounted on the rover, as illustrated in Figure 1. However, the methodology presented in this paper is general and is equally applicable to any type of n -jointed rover-mounted manipulator.

Let θ_1 and θ_2 represent the joint angles and l_1 and l_2 denote the link lengths of the manipulator arm. Consider a moving vehicle frame $\{V\}$ with axes $(F\hat{x}, F\hat{y})$ attached to the rover at the front midpoint F . Let the position of the manipulator end-effector E be the primary task variable of interest. Then, the Cartesian coordinates of E with respect to the frame $\{V\}$ can be expressed as

$$\begin{aligned} \hat{x}_e &= l_1 \cos \theta_1 + l_2 \cos(\theta_1 + \theta_2) \\ \hat{y}_e &= l_1 \sin \theta_1 + l_2 \sin(\theta_1 + \theta_2) \end{aligned} \quad (10)$$

The end-effector position coordinates $X_e = [x_e, y_e]^T$ relative to the world frame $\{W\}$ are given by

$$\begin{aligned} x_e &= x_f + l_1 \cos(\theta_1 + \phi) + l_2 \cos(\theta_1 + \theta_2 + \phi) \\ y_e &= y_f + l_1 \sin(\theta_1 + \phi) + l_2 \sin(\theta_1 + \theta_2 + \phi) \end{aligned} \quad (11)$$

From equation (11), the Cartesian velocity of the end-effector in $\{W\}$ is related to the rate-of-change of the configuration variables as

$$\begin{aligned} \dot{x}_e &= \dot{x}_f + l_1(\dot{\theta}_1 + \dot{\phi}) \sin(\theta_1 + \phi) + l_2(\dot{\theta}_1 + \dot{\theta}_2 + \dot{\phi}) \sin(\theta_1 + \theta_2 + \phi) \\ \dot{y}_e &= \dot{y}_f + l_1(\dot{\theta}_1 + \dot{\phi}) \cos(\theta_1 + \phi) + l_2(\dot{\theta}_1 + \dot{\theta}_2 + \dot{\phi}) \cos(\theta_1 + \theta_2 + \phi) \end{aligned} \quad (12)$$

or, in matrix form

$$\begin{bmatrix} 1 & 0 & J_{m13} & J_{m14} & -l_2 \sin \theta_{120} \\ 0 & 1 & J_{m23} & J_{m24} & l_2 \sin \theta_{120} \end{bmatrix} \begin{bmatrix} \dot{X}_f \\ \dot{\phi} \\ \dot{\theta} \end{bmatrix} = \dot{X}_e \quad (13)$$

where $J_{m13} = J_{m14} = -l_1 \sin \theta_{10} - l_2 \sin \theta_{120}$, $J_{m23} = J_{m24} = l_1 \cos \theta_{10} + l_2 \cos \theta_{120}$, $\theta_{10} = \theta_1 + \phi$, $\theta_{120} = \theta_1 + \theta_2 + \phi$, and $\theta = [\theta_1, \theta_2]^T$ is the 2×1 manipulator joint position vector. Equation (13) can be written in the compact form

$$J_m(q)\dot{q} = \dot{X}_e \quad (14)$$

where $J_m(q)$ is the 2×5 manipulator end-effector Jacobian matrix, and $q = [p^T, \theta^T]^T = [x_f, y_f, \phi, \theta_1, \theta_2]^T$ is the 5×1 configuration vector of the rover-mounted manipulator system. Equation (14) represents a *holonomic* kinematic constraint since it can be expressed as the position constraint $H(q) = 0$ in the form of equation (11).

We conclude that the kinematics of the rover-plus-manipulator system can be modeled as the non-holonomic rover constraint

$$J_r(q)\dot{q} = 0 \quad (15)$$

where $J_r(q) = [G(p); 0]$, together with the holonomic manipulator constraint

$$J_m(q)\dot{q} = \dot{X}_e \quad (16)$$

Equations (15) and (16) can be combined to obtain the differential kinematic model of the integrated rover-plus-manipulator system as

$$\begin{bmatrix} J_r(q) \\ J_m(q) \end{bmatrix} \dot{q} = \begin{bmatrix} 0 \\ \dot{X}_e \end{bmatrix} \quad (17)$$

2 . 3 Motion Control of Integrated Rover-plus-Manipulator System

In this section, the configuration control methodology developed earlier [14- 15] for redundant manipulators is utilized for motion control of the rover-plus-manipulator system.

Consider the integrated rover-plus-manipulator system. The integrated system is kinematically redundant with the degree-of-redundancy $r = n - m$, where n and m are the dimensions of \dot{q} and $[0, \dot{X}_e^T]^T$ in the general case, respectively. Equation (17) can produce infinite *distinct* rover and manipulator motions $q(t)$ which yield the *same* end-effector trajectory $X_e(t)$ while satisfying the non-holonomic rover constraint. In this paper, we adopt the configuration control approach in which an appropriate motion is chosen from this infinite set which causes the integrated system to accomplish an *additional* user-specified task. This additional task is performed by direct control of a set of r user-defined kinematic functions

$$Z = g(q) \quad (18)$$

while controlling the end-effector motion, where Z and g are $r \times 1$ vectors. The additional task constraint (18) can be expressed in the velocity form

$$J_c(q)\dot{q} = \dot{Z} \quad (19)$$

where $J_c = \frac{\partial g}{\partial q}$ is the $r \times n$ Jacobian matrix associated with the kinematic functions Z . This approach to redundancy resolution is very general since each kinematic function z_i can represent a geometric variable (e.g., coordinate of a point on the system), a physical variable (such as a joint gravity torque), or an abstract mathematical function (e.g., projection of the

gradient of an optimization function). Furthermore, the user is not confined to a fixed set of kinematic functions and can select different z_i depending on the task requirements during the execution of the end-effector motion.

On combining the rover-plus-manipulator constraints (17) and the user-specified additional task constraint (19), we obtain

$$\begin{array}{c} J_r(q) \\ J_m(q) \\ \vdots \\ J_c(q) \end{array} \dot{q} = \begin{bmatrix} 0 \\ \dot{X}_e \\ \dot{Z} \end{bmatrix} \quad (20)$$

or, in matrix form

$$J(q)\dot{q} = \dot{X} \quad (21)$$

where $J(q)$ is the $n \times n$ augmented Jacobian matrix, and $\dot{X} = [0, \dot{X}_e^T, \dot{Z}^T]^T$ is the $n \times 1$ augmented task velocity vector.

Suppose that the desired end-effector velocity \dot{X}_{de} and the desired rate-of-variation of the kinematic functions \dot{Z}_d are specified by the user. Then we need to solve the augmented differential kinematic equation

$$J(q)\dot{q} = \dot{X}_d \quad (22)$$

for q , where $\dot{X}_d = [0, \dot{X}_{de}^T, \dot{Z}_d^T]^T$. To avoid large velocities \dot{q} , the user can impose the velocity weighting factor $W_v = \text{diag}\{W_a, W_b\}$ on $\{\dot{p}, \dot{\theta}\}$, and attempt to minimize the weighted sum-of-squares of velocities $\|\dot{p}\|_{W_a}^2 + \|\dot{\theta}\|_{W_b}^2$. Typically, the rover movement is slower than the arm motion and W_a is larger than W_b . In addition, the user can assign priorities to the end-effector and additional task requirements and non-holonomic rover constraint by selecting the appropriate task weighting factor $W_t = \text{diag}\{W_r, W_e, W_c\}$, and seek to minimize the weighted sum of task velocity errors $\|\dot{E}_r\|_{W_r}^2 + \|\dot{E}_e\|_{W_e}^2 + \|\dot{E}_c\|_{W_c}^2$, where $\dot{E}_r = J_r\dot{q}$, $\dot{E}_e = \dot{X}_{de} - \dot{X}_e$ and $\dot{E}_c = \dot{Z}_d - \dot{Z}$ are the non-holonomic rover, end-effector, and additional task velocity errors, respectively. Hence, we seek to find the optimal solution of equation (22) that minimizes the scalar cost function

$$L = \dot{p}^T W_a \dot{p} + \dot{\theta}^T W_b \dot{\theta} + \dot{E}_r^T W_r \dot{E}_r + \dot{E}_e^T W_e \dot{E}_e + \dot{E}_c^T W_c \dot{E}_c \quad (23)$$

The optimal damped-least-squares solution of (22) that minimizes (23) is given by [15]

$$\dot{q} = [J^T W_t J + W_v]^{-1} J^T W_t \dot{X}_d \quad (24)$$

Note that in the special case where $W_v = 0$, equation (24) gives $\dot{q} = J^{-1} \dot{X}_d$, assuming $\det[J] \neq 0$, which is the inverse Jacobian solution for the augmented equation (22). To correct for task-space trajectory drift which occurs inevitably due to the linearization error inherent in differential kinematic schemes, we introduce the *actual* configuration vector X in equation (24) as [15]

$$\dot{q} = [J^T W_t J + W_v]^{-1} J^T W_t [\dot{X}_d + K(X_d - X)] \quad (25)$$

where K is an $n \times n$ constant diagonal matrix with zero or positive diagonal elements. Notice that for the non-holonomic rover constraint, the appropriate elements of X and X_d are set to zero since the constraint is non-integrable. The introduction of the error correction term $K(X_d - X)$ in (25) provides a “closed-loop” characteristic whereby the difference between the desired and actual configuration vectors is used as a driving term in the inverse kinematic transformation. Note that for task-space trajectories with constant final values, $\dot{X}_d(t) = 0$ for $t \geq \tau$ where τ is the motion duration, and using (24) we obtain $\dot{q}(t) = 0$ for $t \geq \tau$; i.e., the manipulator and rover degrees-of-freedom will cease motion for $t \geq \tau$ and any task tracking-error at $t = \tau$ will continue to exist for $t > \tau$. However, by using (25) the manipulator and rover degrees-of-freedom continue to move for $t \geq \tau$ until the desired configuration vector is reached, i.e., $X \rightarrow X_d$ as $t \rightarrow \infty$, [15]. The value of K determines the rate of convergence of X to X_d .

The proposed dual-least-squares configuration control scheme provides a general and unified framework for motion control of the integrated rover-plus-manipulator system. This scheme allows independent weighting of rover movement and manipulator motion, and enables a wide range of redundancy resolution goals to be accomplished. Note that multiple goals (i.e., $r > (n - m)$) can be defined for redundancy resolution and weighted appropriately based on the current task requirements.

Let us now re-visit the two-jointed manipulator arm mounted on the rover as illustrated in Figure 1. This integrated system has the degree-of-redundancy $r = n - m = 2$, and therefore two configuration-dependent kinematic functions $z_1(q)$ and $z_2(q)$ can be specified and controlled independently of the end-effector motion and the non-holonomic rover constraint. For this system, we choose the rover orientation ϕ relative to the world frame and the manipulator elbow angle ψ between the upper-arm and forearm as the additional task variables. Hence

$$z_1(q) = \phi \quad , \quad z_2(q) = \psi = 180 - \theta_2 \quad (\text{Xi})$$

or, in velocity form

$$\begin{bmatrix} 0 & 0 & 1 & 0 & 0 \\ 0 & 0 & 0 & 0 & -1 \end{bmatrix} \dot{q} = \begin{bmatrix} \dot{\phi}_d \\ \dot{\psi}_d \end{bmatrix} \quad (27)$$

where $\dot{q} = [\dot{x}_f, \dot{y}_f, \dot{\phi}, \dot{\theta}_1, \dot{\theta}_2]^T$, and $\dot{\phi}_d$ and $\dot{\psi}_d$ are the desired rate-of-validation of ϕ and ψ , respectively. On combining the rover plus-manipulator model (17) with the additional task specifications (27), we obtain

$$\left[\begin{array}{ccccc|c} \sin \phi & -\cos \phi & 1 & 0 & 0 & \dot{x}_f \\ 1 & 0 & J_{23} & J_{24} & J_{25} & \dot{y}_f \\ 0 & 1 & J_{33} & J_{34} & J_{35} & \dot{\phi} \\ 0 & 0 & 1 & 0 & 0 & \dot{\theta}_1 \\ 0 & 0 & 0 & 0 & -1 & \dot{\theta}_2 \end{array} \right] = \left[\begin{array}{c} 0 \\ \dot{x}_{de} \\ \dot{y}_{de} \\ \dot{\phi}_d \\ \dot{\psi}_d \end{array} \right] \quad (28)$$

where $J_{23} = J_{24} = -l_1 \sin \theta_{10} - l_2 \sin \theta_{120}$; $J_{33} = J_{34} = l_1 \cos \theta_{10} - l_2 \cos \theta_{120}$; $J_{25} = -l_2 \sin \theta_{120}$; $J_{35} = l_2 \cos \theta_{120}$; $\theta_{10} = \theta_1 + \phi$; $\theta_{120} = \theta_1 + \theta_2 + \phi$. Equation (28) represents a set of five

equations in the five unknown elements of \dot{q} that can be solved using the damped-least-squares configuration control approach described earlier in this section. By direct calculation, the determinant of the 5×5 augmented Jacobian matrix appearing on the left-hand side of (28) is found to be

$$\det[J] = l_1 \cos \theta_1 + l_2 \cos(\theta_1 + \theta_2) \neq 0 \quad (29)$$

Therefore, J is non-singular and (28) can be solved exactly provided that $\hat{x}_e \neq 0$; i.e., the end-effector E does not lie on the $F\hat{y}$ axis of the vehicle frame $\{V\}$.

Now, suppose that the rover length is $l = 20\text{cm}$ and the link lengths are $l_1 = l_2 = 10\text{cm}$. Let the initial configuration of the rover-plus-manipulator system be given by

$$q^i = \{x_f = 30\text{cm}, y_f = 15\text{cm}, \phi = 0^\circ, \theta_1 = -75^\circ, \theta_2 = 150^\circ\}$$

This yields the initial task vector

$$X^i = \{x_e = 35.18\text{cm}, y_e = 15\text{cm}, \phi = 0^\circ, \psi = 30^\circ\}$$

as shown in Figure 2. Suppose that the desired final task vector at time $\tau = 1$ second is specified as (see Figure 2)

$$X^f = \{x_e = 65.18\text{cm}, y_e = 45\text{cm}, \phi = 30^\circ, \psi = 90^\circ\}$$

This corresponds to a rapid end-effector motion of $\{(\Delta x_e)^2 + (\Delta y_e)^2\}^{1/2} = 42.4\text{cm}$ in one second. Notice that the target end-effector position is *not* attainable without rover motion. Task-space motion trajectories are specified as

$$x_d(t) = \begin{cases} x^i + \frac{x^f - x^i}{\tau} \cdot t & , \text{ for } t \leq \tau \\ x^f & , \text{ for } t > \tau \end{cases} \quad (30)$$

where (x^i, x^f) are the initial and final values and τ is the duration of motion. Similar trajectories are specified for $y_d(t)$, $\phi_d(t)$, and $\psi_d(t)$. These trajectories produce a straight-line end-effector motion in Cartesian space from (x_e^i, y_e^i) to (x_e^f, y_e^f) . Notice that the target elbow angle $\psi = 90^\circ$ gives maximum end-effector manipulability at the final configuration.

A computer simulation study is performed to calculate the required configuration variables $q(t) = \{x_f(t), y_f(t), \phi(t), \theta_1(t), \theta_2(t)\}$ to accomplish the tasks of end-effector motion, and ϕ and ψ control, while satisfying the non-holonomic rover constraint. In the simulation, we set $\tau = 1$, $\Delta t = 0.01$, $W = \text{diag}\{1, 1, 1, 1, 1\}$, $W_v = \text{diag}\{0, 0, 0, 0, 0\}$, and $K = \text{diag}\{0, 0.1, 0.1, 0, 0\}$. The simulation results are shown in Figures 3a-3d. The path traversed by the end-effector E is shown in Figure 3a. It is seen that the end-effector moves along a straight line from (x_e^i, y_e^i) to (x_e^f, y_e^f) , as specified. Figure 3b verifies that the rover orientation ϕ and the elbow angle ψ change from their initial values to the specified final values in one second, as desired. The path traversed by the rover front mid-point F and the variations of the arm joint angles θ_1 and θ_2 are depicted in Figures 3c and 3d. The rover non-holonomic constraint function $f = \dot{x}_f \sin \phi - \dot{y}_f \cos \phi - \phi l$ is computed and is found to be equal to zero throughout the motion; i.e., the rover constraint is satisfied. Note that the required rover velocity v and steering angle γ can be computed from equation (9).

3 Motion Control of Mobile Robots with 11 Holonomic Base Constraints

The mobile robots considered in this section consist of a robot manipulator mounted on a mobile base with a holonomic constraint. Although the physical appearance of such mobile robots are completely different, their underlying kinematics principles can be formulated in a similar manner. For these mobile robots, the kinematic constraints of the base platform can be expressed in terms of base position alone, similar to the manipulator kinematics itself. In this case, the base can effectively be treated as additional revolute or prismatic joints of the manipulator. Two common examples of this class are a robot mounted on a track and a compound manipulator where one arm operates from the end of another arm. For this class of mobile robots, the overall manipulator arm-plus-mobile base system can be viewed as a composite of two subsystems: the manipulator arm with n_a degrees-of-freedom, and the mobile base with n_b degrees-of-freedom. The n_a degrees-of-manipulation are often of the revolute joint type. The n_b degrees-of-mobility can be treated as prismatic joints in the case of a tracked robot or as revolute joints in the case of a compound manipulator. Let us define a fixed world frame of reference $\{M'\}$ in the robot workspace, a moving base frame $\{B\}$ attached to the manipulator base, and a moving end-effector frame $\{E\}$ attached to the manipulator end-effector. The end-effector frame $\{E\}$ is related to the base frame $\{B\}$ by the 4x4 homogeneous transformation matrix $T_B^E(\theta_a)$, which is the product of the arm joint-to-joint transforms. The transformation that relates the base frame $\{B\}$ to the world frame $\{W\}$ is denoted by $T_W^B(\theta_b)$, and is obtained by multiplying the base interjoint transforms. Thus, the end-effector frame $\{E\}$ is related to the world frame $\{W\}$ by the 4x4 homogeneous transformation matrix

$$T_W^E = T_W^B(\theta_b) \cdot T_B^E(\theta_a) = \begin{pmatrix} R & p \\ 0 & 1 \end{pmatrix} \quad (31)$$

where $R = \{r_{ij}\}$ is the 3x3 end-effector rotation matrix and $p = [x, y, z]^T$ is the end-effector position vector, both with respect to the world frame $\{W\}$. One common three-parameter representation of the end-effector orientation is the equivalent angle-axis $\beta\hat{k} = [\hat{k}_x, \hat{k}_y, \hat{k}_z]^T$ which can be extracted readily from the rotation matrix R , [16]. Therefore, the $m (\leq 6)$ end-effector position and orientation coordinates to be controlled can be obtained from (31) and represented by the $m \times 1$ Vector

$$Y = f(\theta_a, \theta_b) \quad (32)$$

Equation (32) describes the forward kinematic model that relates the arm and base joint coordinates $\{O, \theta_a, \theta_b\}$ to the end-effector Cartesian coordinates Y in the fixed world frame $\{W\}$. The differential kinematic model that relates the end-effector Cartesian velocity \dot{Y} to the arm and base joint velocities $\{\dot{\theta}_a, \dot{\theta}_b\}$ is given by

$$\dot{Y} = [J_a(\theta) \vdots J_b(\theta)] \begin{bmatrix} \dot{\theta}_a \\ \dots \\ \dot{\theta}_b \end{bmatrix} = J_e(\theta)\dot{\theta} \quad (33)$$

where $J_a(\theta) = \frac{\partial f}{\partial \theta_a}$ and $J_b(\theta) = \frac{\partial f}{\partial \theta_b}$ are the $m \times n_a$ and $m \times n_b$ Jacobian matrices of the arm and the base, respectively¹, $\theta = \begin{bmatrix} \theta_a \\ \theta_b \end{bmatrix}$ is the $n \times 1$ vector of mobility and manipulation joints, and $n = n_a + n_b$. This formulation puts the n_b mobility and the n_a manipulation degrees-of-freedom on the same footing, and treats both θ_a and θ_b equally within a common framework. Equations (32) and (33) describe the kinematics of a composite robotic system with n joint degrees-of-freedom operating in an m -dimensional Cartesian task space.

Before discussing coordinated control of mobility and manipulation, let us investigate the effect of base mobility on the end-effector manipulability index in the common case where the total joint degrees-of-freedom n exceeds the end-effector task dimension m . When the base is stationary, the end-effector manipulability index due to the arm joints $\{O_a\}$ is defined as [18]

$$\mu_a(\theta) = \{\det[J_a(\theta)J_a^T(\theta)]\}^{1/2} \quad (34)$$

Note that in any non-singular arm configuration, $J_a(\theta)J_a^T(\theta)$ is a symmetric positive-definite matrix whose determinant is a positive function of $\{\theta_a\}$. Now, when base mobility is introduced, the end-effector Jacobian matrix changes from J_a to $J_e = [J_a \vdots J_b]$, and the end-effector manipulability index due to both arm and base joints $\{O_e\} = \{\theta_a, \theta_b\}$ is obtained as

$$\begin{aligned} \mu_e(\theta) &= \{\det[J_e(\theta)J_e^T(\theta)]\}^{1/2} \\ &= \{\det[J_a(\theta)J_a^T(\theta) \vdash J_b(\theta)J_b^T(\theta)]\}^{1/2} \end{aligned} \quad (35)$$

In the Appendix, it is shown that

$$\mu_e(\theta) = \mu_a(\theta) + \sigma(\theta) \quad (36)$$

where $\sigma(\theta)$ is a *positive* function of O_e . Equation (36) implies that the base mobility always enhances the end-effector manipulability index. This is expected in view of the fact that the base degrees-of-freedom contribute to the end-effector motion and thereby increase the Cartesian mobility of the end-effector. At singular arm configurations, $J_a(0)$ is rank-deficient and $\mu_a(\theta) = 0$. As shown in the Appendix, in this case $\mu_e(\theta) \geq \mu_a(\theta)$; that is the base mobility can in general increase the end-effector manipulability index, however in certain

¹In practice, J_a and J_b are computed using the **vector** cross-product formula due to Whitney [10].

cases $\mu_c(0)$ is also equal to zero. We conclude that in general, the end-effector manipulability index is increased by the presence of base mobility.

Let us now consider the coordinated control of the composite arm-plus-base system. The composite system is kinematically redundant with the degree-of-redundancy $r = n - m$. Following the configuration control approach outlined in Section 2.3, the redundancy is utilized so that the mobile robot satisfies a set of r kinematic constraints

$$z_i(\theta) = z_{di}(t) \quad i = 1, \dots, r \quad (37)$$

while executing the desired end-effector motion, where $z_i(\theta)$ is a user-defined kinematic function of the mobile robot configuration O , and $z_{di}(t)$ is the user-specified desired time variation of z_i . Equation (37) can be written in the velocity form

$$\dot{z}_i(\theta) = J_{ci}(\theta)\dot{\theta} = \dot{z}_{di}(t) \quad (38)$$

where $J_{ci} = \frac{\partial z_i}{\partial \theta}$ is the $1 \times n$ Jacobian matrix related to the kinematic function z_i . The augmented differential kinematic model of the manipulator arm-plus-mobile base system is therefore obtained as

$$\begin{pmatrix} \dot{Y}(t) \\ \dot{Z}(t) \end{pmatrix} = \begin{pmatrix} J_o(\theta) & \vdots & J_b(\theta) & \dot{\theta}_a \\ \dots & \dots & \dots & \dots \\ J_c(\theta) & & & \dot{\theta}_b \end{pmatrix} \begin{pmatrix} \dot{\theta}_a \\ \dot{\theta}_b \end{pmatrix} = J(\theta)\dot{\theta} \quad (39)$$

where $J_c(\theta) = \frac{\partial Z}{\partial \theta}$ is the $r \times n$ Jacobian matrix associated with the kinematic functions Z , and $J(\theta)$ is the $n \times n$ augmented Jacobian matrix. This formulation puts the redundancy resolution goal on the same footing as the end-effector task, and treats both Y and Z equally in a common format. Now, to find the base movement and arm motion that meet the end-effector specification $Y(O) = Y_d(t)$ and the kinematic constraints $Z_i(\theta) = Z_d(t)$, we need to solve the augmented differential kinematic equation (39) for $\dot{\theta}$, given $\dot{Y}_d(t)$ and $\dot{Z}_d(t)$. As in Section 2.3, to avoid large joint velocities, the user can impose the velocity weighting factor $W_v = \text{diag}\{W_a, W_b\}$ on $\{\dot{\theta}_a, \dot{\theta}_b\}$, and furthermore can assign priorities to the different tasks requirements by selecting the appropriate task weighting factor $W_t = \text{diag}\{W_e, W_c\}$. The closed-loop optimal least-squares solution of (39) is given by [15]

$$\dot{\theta} = [J^T W_t J + W_v]^{-1} J^T W_t [\dot{X}_d + K(X_d - X)] \quad (40)$$

where K is the position feedback gain matrix introduced to correct for task-space trajectory drift due to the linearization error. For digital control implementation, equation (40) is discretized as

$$\frac{\theta(N+1) - \theta(N)}{\Delta t} = [J^T W_t J + W_v]^{-1} J^T W_t \left[\frac{X_d(N+1) - X_d(N)}{\Delta t} + KX_d(N) - KX(N) \right] \quad (41)$$

or

$$\theta(N+1) = \theta(N) + [J^T W_t J + W_v]^{-1} J^T W_t [X_d(N+1) - (1 - K\Delta t) X_d(N) - K\Delta t X(N)] \quad (42)$$

where N denotes the sampling instant and Δt is the sampling period. Equation (42) is used to compute $\theta(N+1)$ given $\{\theta(N), X_d(N+1), X_d(N), X(N)\}$. Note that in the special case when $K = \frac{1}{\Delta t} f$, where f is the sampling frequency, equation (42) simplifies to

$$\theta(N+1) = \theta(N) + [J^T W_t J + W_v]^{-1} J^T W_t [X_d(N+1) - X(N)] \quad (43)$$

This equation can be considered as the discrete-time version of (42) with $K = 0$ and the desired position $X_d(N)$ replaced by the *actual* position $X(N)$ to correct for drift. Notice that, in practice, the inversion of the positive-definite matrix $[J^T W_t J + W_v]$ is not needed, and $\theta(N+1)$ can be found using the Cholesky decomposition.

In summary, the procedure for coordinated control of base mobility and arm manipulation is as follows:

(i) Augment by column the arm Jacobian J_a with the last Jacobian J_b to obtain the overall end-effector Jacobian $J_e = [J_a; J_b]$. Note that the availability of base mobility appears as extra columns in the Jacobian matrix, since in effect it increases the dimension of the joint space.

(ii) Augment by row the end-effector Jacobian J_e with the constraint Jacobian J_c which relates to the user-defined additional task to be accomplished due to kinematic redundancy.

This yields the augmented Jacobian $J = \begin{bmatrix} J_e \\ \vdots \\ J_c \end{bmatrix}$. Note that the additional task leads to extra rows in the Jacobian matrix, since it effectively increases the dimension of the task space.

(iii) Specify the end-effector and constraint task weighting factors $W_t = \text{diag}\{W_e, W_c\}$, the arm and base joint velocity weighting factors $W_v = \text{diag}\{W_a, W_b\}$, and the position feedback gain K .

(iv) Use the closed-loop `cl111)cc:cl-least-scl-lales` approach to find the optimal arm and base motions as $\dot{\theta} = [J^T W_t J + W_v]^{-1} J^T W_t [X_d + K(X_d - X)]$.

For the sake of illustration, we shall now consider a spatial three-jointed arm mounted on a one DOF mobile platform, as shown in Figure 4. This resembles a PUMA robot (without the wrist,) mounted on a rail to obtain base inmobility. Let us denote the waist joint by θ_1 , the shoulder joint by θ_2 , the elbow joint by θ_3 , and let θ_4 represent the platform mobility in x -direction, treated as a prismatic joint. Let us first assume that the robot base is stationary, i.e. $\dot{\theta}_4 = 0$. The forward kinematic model relating the joint angles $O = (\theta_1, \theta_2, \theta_3)^T$ to the tip Cartesian coordinates $Y = (x, y, z)^T$ in the reference world frame are readily found to be

$$x = \ell \cos \theta_1 [\sin \theta_2 - \sin(\theta_2 + \theta_3)]$$

$$\begin{aligned}y &= \ell \sin \theta_1 [\sin \theta_2 + \sin(\theta_2 + \theta_3)] \\z &= \ell [\cos \theta_2 + \cos(\theta_2 + \theta_3)] + h\end{aligned}\quad (44)$$

where h is the shoulder height and ℓ is the length of the upper-arm or forearm, and is set to unity for simplicity. The differential kinematic model of the robot is $\dot{Y} = J_e(\theta)\dot{\theta}$, where the elements of the 3x3 hand Jacobian matrix are obtained from (44) as

$$\begin{aligned}J_{e11} &= \frac{\partial x}{\partial \theta_1} = -\sin \theta_1 [\sin \theta_2 + \sin(\theta_2 + \theta_3)] ; \quad J_{e12} = \frac{\partial x}{\partial \theta_2} = \cos \theta_1 [\cos \theta_2 + \cos(\theta_2 + \theta_3)] \\J_{e13} &= \frac{\partial x}{\partial \theta_3} = \cos \theta_1 \cos(\theta_2 + \theta_3) ; \quad J_{e21} = \frac{\partial y}{\partial \theta_1} = \cos \theta_1 [\sin \theta_2 + \sin(\theta_2 + \theta_3)] \\J_{e22} &= \frac{\partial y}{\partial \theta_2} = \sin \theta_1 [\cos \theta_2 + \cos(\theta_2 + \theta_3)] ; \quad J_{e23} = \frac{\partial y}{\partial \theta_3} = \sin \theta_1 \cos(\theta_2 + \theta_3) \\J_{e31} &= \frac{\partial z}{\partial \theta_1} = 0 ; \quad J_{e32} = \frac{\partial z}{\partial \theta_2} = -\sin \theta_2 - \sin(\theta_2 + \theta_3) ; \quad J_{e33} = \frac{\partial z}{\partial \theta_3} = -\sin(\theta_2 + \theta_3)\end{aligned}$$

The singular configurations of the arm are found from

$$\det[J] = \sin \theta_3 [\sin \theta_2 + \sin(\theta_2 + \theta_3)] \quad (45)$$

as

$$1: \begin{array}{ll} \sin \theta_3 = 0 & \rightarrow \theta_3 = 0^\circ \text{ arm fully extended} \\ \text{elbow singularity} & \theta_3 = 180^\circ \text{ arm fully folded} \end{array}$$

$$11: \begin{array}{ll} \sin \theta_2 + \sin(\theta_2 + \theta_3) = 0 & \rightarrow x = y = 0 \text{ hand is straight above} \\ \text{shoulder singularity} & \text{the shoulder} \end{array}$$

Note that the case 1 singularities correspond to the hand on the outer ($\theta_3 = 0^\circ$) or inner ($\theta_3 = 180^\circ$) workspace boundary, and in case 11 the joint θ_1 does not affect (x, y, z) of the hand and hence a joint DOP is ineffective. The above results are the classical singularities of the PUMA arm which are well-known and are repeated here for comparison with the mobile platform Case.

Now, let us introduce base mobility to the system through the prismatic joint θ_4 . Since θ_4 is along the x-axis, we obtain

$$x = \ell \cos \theta_1 [\sin \theta_2 + \sin(\theta_2 + \theta_3)] + \theta_4 \quad (46)$$

but y and z in equation (44) are not affected. The new hand Jacobian J_e will now be a 3x4 matrix with the fourth column as

$$J_{e14} = \frac{\partial x}{\partial \theta_4} = 1 ; \quad J_{e24} = \frac{\partial y}{\partial \theta_4} = 0 ; \quad J_{e34} = \frac{\partial z}{\partial \theta_4} = 0 \quad (47)$$

Let us now consider the coordinated control of the arm and the platform. The robotic system in Figure 4 is kinematically redundant since infinite combinations of joint motions $\theta = (\theta_1, \theta_2, \theta_3, \theta_4)^T$ can produce the same tip trajectory $Y = (x, y, z)^T$. This redundancy is

resolved by picking out an appropriate solution from this infinite set that meets a user-defined additional task requirement. In this case study, we define the “elbow angle” ϕ between the upper-arm and forearm as the kinematic function to be controlled independently of the tip position for redundancy resolution. The elbow angle $\phi = 180^\circ + \theta_3$ determines the “reach” of the arm AP, since

$$AP = \ell \sin \phi / 2 + \ell \sin \phi / 2 = 2 \sin \phi / 2 \quad (48)$$

Hence by controlling ϕ we can directly influence the reach of the arm. By introducing the elbow angle ϕ as the fourth task variable, the forward and differential kinematic models of the robot are augmented by

$$\phi(\theta) = 180^\circ - \theta_3 \quad (49)$$

$$J_c(\theta) = \frac{\partial \phi}{\partial \theta} = [0, 0, 1, 0] \quad (50)$$

Hence, the 4×4 augmented Jacobian matrix relating the rate of change of task variables to the joint velocities has the following structure

$$\begin{pmatrix} \dot{x} \\ \dot{y} \\ \dot{z} \\ \dot{\phi} \end{pmatrix} = \begin{pmatrix} J_{e11} & J_{e12} & J_{e13} & 1 \\ J_{e21} & J_{e22} & J_{e23} & 0 \\ 0 & J_{e32} & J_{e33} & 0 \\ 0 & 0 & 1 & 0 \end{pmatrix} \begin{pmatrix} \dot{\theta}_1 \\ \dot{\theta}_2 \\ \dot{\theta}_3 \\ \dot{\theta}_4 \end{pmatrix} = J \begin{pmatrix} \dot{\theta}_1 \\ \dot{\theta}_2 \\ \dot{\theta}_3 \\ \dot{\theta}_4 \end{pmatrix} \quad (51)$$

Notice that the Jacobian matrix J has a particular structure, with zero elements indicating that some joint angles have no effect on certain task variables. In order to control the task variables (x, y, z, ϕ) independently, the augmented Jacobian matrix J must be non-singular. The singularities of J are found from

$$\det[J] = -J_{e21}J_{e32} = \cos \theta_1 [\sin \theta_2 + \sin(\theta_2 + \theta_3)]^2 \quad (52)$$

Note that the simplicity of $\det[J]$ is a consequence of the particular structure of J . From (52), it is seen that J is singular when:

$$\text{I: } \cos \theta_1 = 0 \quad \rightarrow \quad \theta_1 = 90^\circ, 270^\circ \quad \rightarrow x = \theta_4 \\ \text{Last singularity}$$

$$\text{II: } \sin \theta_2 + \sin(\theta_2 + \theta_3) = 0 \quad \rightarrow \quad x = \theta_4, y = 0 \\ \text{shoulder singularity}$$

To investigate these singularities, we study the augmented Jacobian matrix in these singular configurations. At the singular condition I, the tip and the last have the same x -coordinate, i.e., the tip-base line is perpendicular to the x -axis. In this case, the first and fourth columns of J become multiples of one another; hence θ_1 and θ_4 have identical incremental effects on the task variables $\{x, y, z, \phi\}$. At the singular condition II, the tip is right above the base,

and in this case the first column of J becomes zero; hence θ_1 has no instantaneous effect on any of the task variables $\{x, y, z, \phi\}$ in this configuration.

In comparison with the previous case for the stationary-base robot, it is seen that the base mobility has alleviated the elbow singularity ($\sin \theta_3 = 0$), i.e., the arm is no longer singular when it is fully extended or fully folded. However a new singularity has been introduced ($\cos \theta_1 = 0$) when the tip and the base line up; which is not a classical PUMA singularity and is due to the additional task variable ϕ . Note that if the platform position θ_4 is chosen as the additional task variable instead of the elbow angle ϕ , i.e., the platform position is commanded

$$\begin{vmatrix} & & & & :1 \\ & J_e & & & :0 \\ & & & & :0 \\ & \dots & \dots & \dots & :1 \\ 0 & 0 & 0 & 0 & :1 \end{vmatrix}$$

and controlled directly, then the augmented Jacobian becomes $J =$

and $\det J = \det J_e$; hence the PUMA classical singularities are encountered in this case.

Suppose that we specify desired motion trajectories for the hand coordinates and the elbow angle as $X_d(t) = [x_d(t), y_d(t), z_d(t), \phi_d(t)]^T$. Then the required joint motions are obtained by solving the equation

$$\begin{pmatrix} \dot{x}_d(t) \\ \dot{y}_d(t) \\ \dot{z}_d(t) \\ (\dot{\phi}_d(t)) \end{pmatrix} = \begin{pmatrix} -\sin \theta_1 [\sin \theta_2 + \sin(\theta_2 + \theta_3)] \cos \theta_1 [\cos \theta_2 + \cos(\theta_2 + \theta_3)] & \cos \theta_1 \cos(\theta_2 + \theta_3) & 1 \\ \cos \theta_1 [\sin \theta_2 + \sin(\theta_2 + \theta_3)] & \sin \theta_1 [\cos \theta_2 + \cos(\theta_2 + \theta_3)] & \sin \theta_1 \cos(\theta_2 + \theta_3) & 0 \\ 0 & -\sin \theta_2 - \sin(\theta_2 + \theta_3) & -\sin(\theta_2 + \theta_3) & 0 \\ 0 & 0 & 1 & 0 \end{pmatrix} \begin{pmatrix} \dot{\theta}_1 \\ \dot{\theta}_2 \\ \dot{\theta}_3 \\ \dot{\theta}_4 \end{pmatrix} \quad (53)$$

The closed-loop damped-least-squares solution of (53) that minimizes

$$L = \|\dot{X}_d - J\dot{\theta}\|_{W_t}^2 + \|\dot{\theta}\|_{W_v}^2 \quad (54)$$

is given by

$$\dot{\theta} = [J^T W_t J + W_v]^{-1} J^T W_t [\dot{X}_d + k(X_d - X)] \quad (55)$$

Suppose that initially, the arm joint angles are $\theta_1 = 0^\circ$, $\theta_2 = 90^\circ$, $\theta_3 = -30^\circ$ and the base is at $0.4 = 1.0$ meter relative to a fixed world frame; yielding the initial hand position $x_i = 2.866$ meter, $y_i = 0$ meter, $z_i = 1.5$ meter and the initial elbow angle $\phi_i = 150^\circ$. Let the target task-space arm configuration be specified as $x_f = 3.866$ meter, $y_f = 0.5$ meter, $z_f = 2.25$ meter, and $\phi_f = 90^\circ$ in the world frame. This corresponds to the hand motion of $\|Y_f - Y_i\| = 1.35$ meter in Cartesian space and the elbow angle change of $\phi_f - \phi_i = -60^\circ$. Notice that the target hand position is *not* attainable without last motion, i.e., (x_f, y_f, z_f) is outside the arm workspace when the base is stationary at 1.0 meter. Motion trajectories are specified in task-space as

$$x_d(t) = \begin{cases} x_i + \frac{x_f - x_i}{\tau} t, & \text{for } t \leq \tau \\ x_f, & \text{for } t > \tau \end{cases}; y_d(t) = \begin{cases} y_i + \frac{y_f - y_i}{\tau} t, & \text{for } t \leq \tau \\ y_f, & \text{for } t > \tau \end{cases}$$

$$z_d(t) = \begin{cases} z_i + \frac{z_f - z_i}{\tau} t, & \text{for } t \leq \tau \\ z_f, & \text{for } t > \tau \end{cases}; \phi_d(t) = \begin{cases} \phi_i + \frac{\phi_f - \phi_i}{\tau} t, & \text{for } t \leq \tau \\ \phi_f, & \text{for } t > \tau \end{cases} \quad (56)$$

where τ is the duration of motion. These trajectories produce a straight-line motion in Cartesian space from (x_i, y_i, z_i) to (x_f, y_f, z_f) , since $\frac{x_f - x_i}{x_f - x_i} = \frac{y_f - y_i}{y_f - y_i} = \frac{z_f - z_i}{z_f - z_i}$. To find out the required joint motions, we substitute the desired task velocities

$$\dot{x}_d(t) = \begin{cases} \frac{x_f - x_i}{\tau} & t \leq \tau \\ 0 & t > \tau \end{cases}; \quad \dot{y}_d(t) = \begin{cases} \frac{y_f - y_i}{\tau} & t \leq \tau \\ 0 & t > \tau \end{cases} \quad (57)$$

$$\dot{z}_d(t) = \begin{cases} \frac{z_f - z_i}{\tau} & t \leq \tau \\ 0 & t > \tau \end{cases}; \quad \dot{\phi}_d(t) = \begin{cases} \frac{\phi_f - \phi_i}{\tau} & t \leq \tau \\ 0 & t > \tau \end{cases}$$

into equation (53) and integrate the acquired solution given by equation (55). The Jacobian matrix in (53) is then updated and the procedure is repeated. In this case study, the trajectory duration τ is 1 second, the time increment Δt is 0.01 second, the position feedback gain k is set to 10, and the units of (x, y, z, ϕ) are meters and radian.

Two computer simulation studies are performed to investigate the effects of the base velocity weighting α and the additional task weighting β on the system performance, where $W_v = diag\{0, 0, 0, \alpha\}$ and $W_t = diag\{1, 1, 1, \beta\}$. Notice that in the cost function (54), the arm joint velocities ($\theta_1, \theta_2, \theta_3$) are not penalized and the task velocity error weightings for (x, y, z) are set equal to one.

Case 1 - Effect of α : In this case, we set $\beta = 1$ and find the required joint motions for three different values of the base velocity weighting $\alpha = 0, 1, 10$. Figures 5a-5h depict the computer simulation results and Table 1 summarizes the steady-state values. It is seen that when $\alpha = 0$, the configuration variables (x, y, z, ϕ) track the desired trajectories and reach the target values in $t = 1$ second. For $\alpha = 1$ and $\alpha = 10$, the task-space tracking performance is degraded, but the joints continue to move after $t = 1$ second until the target values are reached ultimately. However, due to the penalty imposed on the base motion, the base moves slower and by a less amount in this case. Notice that a higher value for α results in less base motion but a poorer task-space tracking performance.

Case 2- Effect of α and β : In this case, we choose β a function of α so that as we impose penalty on the last motion, we also relax the additional task constraint. This suggests that β must be an inverse function of α , and here we choose a simple function as $\beta = 1/(\alpha + 1)$. Equation (55) is now solved for three different values of the base velocity weighting $\alpha = 0, 1, 10$ with the corresponding elbow angle weighting $\beta = 1, 0.5, 0.091$. The simulation results are

shown in Figures 6a-6h, and the steady-state values are given in Table 2. It is seen that as α increases and β decreases, the base motion is reduced but the task performance is also degraded. However, since the ϕ constraint is relaxed automatically in this case, we observe a better tracking performance in the hand coordinates (x, y, z) , as compared to the previous case. Recall that since (x_f, y_f, z_f) is outside the robot workspace if the base is stationary, base movement is necessary even if only hand motion is specified.

4 Experimental Study

In this section, we describe the experimental validation of the proposed approach to motion control of mobile robots as applied to a tracked robot. The facility used for this experimental study is the JJ's, Remote Surface Inspection Laboratory. The laboratory setup is shown in Figure 7 and is comprised of a Robotics Research Corporation 1{1'207 seven DOF arm/control unit, a VME-based chassis with two MC68040 processor boards and additional interface cards, two joysticks, a motorized platform/control unit, and a Silicon Graphics IRI S workstation. To enable inspection of extended surfaces, the 1' DOF RRC arm which carries the inspection sensors is mounted on the 1 DOF mobile platform that can move back and forth along a track installed on the floor.

We first describe the kinematic analysis of the system and then present the experimental results.

4.1 Kinematic Analysis

In order to simplify the analysis, we disregard the three minor joints at the wrist and consider the four major joints of the RRC arm; namely the shoulder roll and pitch joints θ_1, θ_2 , and the elbow roll and pitch joints θ_3, θ_4 as shown in Figure 8. The base platform motion on the track is along the x-axis of the world frame and is treated as the prismatic joint θ_5 . Let the task variables of interest be the wrist Cartesian coordinates $\{x, y, z\}$ and the arm angle ψ , defined as the angle between the plane passing through the arm and the vertical plane passing through the shoulder-wrist line. The forward kinematic model relating $\{x, y, z, \psi\}$ to $\{\theta_1, \theta_2, \theta_3, \theta_4, \theta_5\}$ has been found to be [19]

$$\begin{aligned} x &= c_1 s_2 + c_1 s_2 c_4 + s_4(c_1 c_2 c_3 - s_1 s_3) + \theta_5 \\ y &= s_1 s_2 + s_1 s_2 c_4 + s_4(s_1 c_2 c_3 + c_1 s_3) \\ z &= c_2 + c_2 c_4 - s_2 c_3 s_4 + d \\ \psi &= \text{atan2}\{s_2 s_3 s_4, \frac{s_4}{r}[c_2 s_4 + s_2 c_3(1 + c_4)]\} = \text{atan2}\{u, v\} \end{aligned} \quad (58)$$

where u and v are the arguments of the atan2 function, $r = (2 + 2c_4)^{1/2}$ denotes the reach of the arm (i.e., the shoulder-wrist distance SW), h is the shoulder height, the upper-arm

and forearm lengths are taken to be unity ($SE \approx EW \approx 1$), and $s_i = \sin \theta_i$, $c_i = \cos \theta_i$. In deriving equation (58), the small offsets at the shoulder and elbow joints of the arm are ignored relative to the link lengths so that the analysis is mathematically tractable. Note that when there is no elbow roll motion ($\theta_3 = 0$), we obtain $\psi = 0$, i.e., the arm stays in the vertical plane, (58) reduces to (44), and the PUMA robot in Section 3 is retrieved.

Since the robot system shown in Figure 8 has five independent joint degrees-of-freedom, we can control another task variable in addition to $\{x, y, z, \psi\}$. In this study, the additional task variable is chosen as the “elbow angle” ϕ formed between the upper-arm SE and the forearm EW , as in Section 3. The elbow angle ϕ is related to the joint angles by

$$\phi = 180^\circ - 10, \quad (59)$$

and determines the reach of the arm. From triangle WEF , we obtain

$$r = SW = 2\ell \sin \phi/2 = 2 \sin \phi/2 \quad (60)$$

Hence the arm reach r is a simple sinusoidal function of the elbow angle ϕ , and ϕ can be used to control r directly. This equation can also be obtained by applying the cosine law to the SEW triangle to obtain $r = [2 + 2\cos\theta_4]^{1/2}$ which can be reduced to equation (60) using the half-angle cosine formula. Notice that the arm angle ψ and the elbow angle ϕ represent two independent configuration parameters for the arm. The radius of the circle traversed by the elbow when the arm is executing a self-motion (i.e., wrist is fixed) is a function of the elbow angle as $EF = \ell \cos \phi/2$. The variation of the arm reach r as a function of the elbow angle ϕ is shown in Figure 9. It is seen that when ϕ changes in the range $\{0, 180^\circ\}$, r varies from 0 to 2; with $r = 0$ at $\phi = 0$ (arm fully folded) and $r = 2$ at $\phi = 180^\circ$ (arm fully extended).

Equations (58)-(59) represent the augmented forward kinematic model of the mobile robot system. The augmented differential kinematic model relating the joint velocities $\{\dot{\theta}_1, \dot{\theta}_2, \dot{\theta}_3, \dot{\theta}_4, \dot{\theta}_5\}$ to the resulting task variable velocities $\{\dot{x}, \dot{y}, \dot{z}, \dot{\psi}, \dot{\phi}\}$ is obtained by differentiating (58)-(59) as

$$\dot{X} = \begin{pmatrix} \dot{x} \\ \dot{y} \\ \dot{z} \\ \dot{\psi} \\ \dot{\phi} \end{pmatrix} = \begin{pmatrix} J_{11} & J_{12} & J_{13} & J_{14} & : & 1 \\ J_{21} & J_{22} & J_{23} & J_{24} & : & 0 \\ 0 & J_{32} & J_{33} & J_{34} & : & 0 \\ 0 & J_{42} & J_{43} & J_{44} & : & 0 \\ \dots & \dots & \dots & \dots & : & 0 \\ 0 & 0 & 0 & 1 & : & 0 \end{pmatrix} \begin{pmatrix} \dot{\theta}_1 \\ \dot{\theta}_2 \\ \dot{\theta}_3 \\ \dot{\theta}_4 \\ \dot{\theta}_5 \end{pmatrix} = J(\theta) \begin{pmatrix} \dot{\theta}_1 \\ \dot{\theta}_2 \\ \dot{\theta}_3 \\ \dot{\theta}_4 \\ \dot{\theta}_5 \end{pmatrix} \quad (61)$$

Because of the particular structure of the 5x5 augmented Jacobian matrix J , the expression for $\det[J]$ simplifies considerably to

$$\det[J] = -J_{21}[J_{33}J_{42} - J_{32}J_{43}] \quad (62)$$

The elements of J that appear in (62) can be obtained from (58) as

$$\begin{aligned} J_{21} &= \frac{\partial y}{\partial \theta_1} = c_1 s_2 + c_1 s_2 c_4 + c_1 c_2 c_3 s_4 - s_1 s_3 s_4 = x - \theta_5 \\ J_{32} &= \frac{\partial z}{\partial \theta_2} = -s_2 - s_2 c_4 - c_2 c_3 s_4 = -PQ \\ J_{33} &= \frac{\partial z}{\partial \theta_3} = s_2 s_3 s_4 \\ J_{42} &= \frac{\partial \psi}{\partial \theta_2} = \frac{\partial \psi}{\partial u} \cdot \frac{\partial u}{\partial \theta_2} + \frac{\partial \psi}{\partial v} \cdot \frac{\partial v}{\partial \theta_2} = \frac{1}{u^2 + v^2} \left[v \frac{\partial v}{\partial \theta_2} - u \frac{\partial u}{\partial \theta_2} \right] \\ J_{43} &= \frac{\partial \psi}{\partial \theta_3} = \frac{\partial \psi}{\partial u} \cdot \frac{\partial u}{\partial \theta_3} + \frac{\partial \psi}{\partial v} \cdot \frac{\partial v}{\partial \theta_3} = \frac{1}{u^2 + v^2} \left[v \frac{\partial v}{\partial \theta_3} - u \frac{\partial u}{\partial \theta_3} \right] \end{aligned}$$

where $PQ = (x^2 + y^2)^{1/2}$ is the distance between the wrist projection on the x - y plane P and the robot base Q , and the partial derivatives in the above expressions are given by

$$\begin{aligned} \frac{\partial u}{\partial \theta_2} &= c_2 s_3 s_4 ; \quad \frac{\partial v}{\partial \theta_2} = \frac{s_4}{r} [s_2 s_4 + c_2 c_3 (1 + c_4)] \\ \frac{\partial u}{\partial \theta_3} &= s_2 c_3 s_4 ; \quad \frac{\partial v}{\partial \theta_3} = \frac{s_4}{r} [-s_2 s_3 (1 + c_4)] \end{aligned}$$

Substituting these expressions into (62) and simplifying the result yields the surprisingly simple expression

$$\det[J] = rs_2(\theta_5 - x) \quad (63)$$

This analysis shows that the arm-plus-platform system has the following singular configurations:

- 1 : $\theta_5 - x = 0 \rightarrow x = \theta_5$ wrist and platform have the same x -coordinate
- 11: $s_2 = 0 \rightarrow \theta_2 = 0^\circ, 180^\circ$ upper-arm is vertical
- 111: $r = 0 \rightarrow \theta_4 = 180^\circ$ arm is fully folded

In singular configuration I (i.e., $x = 05$), the first and fifth columns of J are multiples and hence θ_1 and θ_5 have identical effects on the task variables. In singular configurations 11 and 111 (i.e., $s_2 = 0$ and $c_4 = -1$), the 2×2 submatrix $\begin{pmatrix} J_{32} & J_{33} \\ J_{42} & J_{43} \end{pmatrix}$ of J becomes rank-deficient, and hence the joint angles $\{\theta_2, \theta_3\}$ do not affect the task variables $\{z, \psi\}$ independently.

4.2 Experimental Results

Suppose that the motion trajectories $X_d(t) = [x_d(t), y_d(t), z_d(t), \psi_d(t), \phi_d(t)]^T$ are specified for the task variables. Then the required joint motions can be obtained by finding the closed-loop clairfil(~cl- least- scillalt's solution of

$$\dot{X}_d = \begin{pmatrix} \dot{x}_d \\ \dot{y}_d \\ \dot{z}_d \\ \dot{\psi}_d \\ \dot{\phi}_d \end{pmatrix} = \begin{pmatrix} J_{11} & J_{12} & J_{13} & J_{14} & 1 \\ J_{21} & J_{22} & J_{23} & J_{24} & 0 \\ 0 & J_{32} & J_{33} & J_{34} & 0 \\ 0 & J_{42} & J_{43} & J_{44} & 0 \\ 0 & 0 & 0 & 1 & 0 \end{pmatrix} \begin{pmatrix} \dot{\theta}_1 \\ \dot{\theta}_2 \\ \dot{\theta}_3 \\ \dot{\theta}_4 \\ \dot{\theta}_5 \end{pmatrix} = JO \quad (64)$$

that minimizes the cost function $L = \|\dot{X}_d - J\dot{\theta}\|_{W_t}^2 + \|\dot{\theta}\|_{W_v}^2$ as

$$\dot{\theta} = [J^T W_t J + W_v]^{-1} J^T W_t [\dot{X}_d - K(X_d - X)] \quad (65)$$

Typically, the pitch angle θ_4 can vary in the range $-180^\circ \leq \theta_4 \leq 0^\circ$ and hence the range of variation of the elbow angle ϕ is 0° to 180° . The most desirable elbow angle is $\phi = 90^\circ$, which corresponds to the pitch angle θ_4 in mid-range and ensures that the arm is not in an over-stretched ($\phi \approx 180^\circ$) or an under-stretched ($\phi \approx 0^\circ$) configuration. The elbow condition $\phi = 90^\circ$ can also be derived from another point of view. For the robot arm shown in Figure 8, the upper-arm *SE* and forearm *EW* define the arm plane Δ . The robot can be viewed as a two-link planar arm with joint rotations θ_2 and θ_4 which move the arm in the plane Δ . The arm plane Δ can rotate about the shoulder roll axis by θ_1 and about the upper-arm by θ_3 . When the robot base is stationary ($\theta_5 = 0$), the wrist attains *maximum manipulability* when $\theta_2, \theta_4 = 90^\circ$, which is the classical two-link arm result [18]. Hence ensuring that the elbow angle $\phi = 90^\circ$ guarantees the optimality of the wrist manipulability in the arm plane Δ when $\theta_5 = 0$.

Having established the desirability of the $\phi = 90^\circ$ condition based on the above arguments, the platform can be positioned continuously to attain the target elbow angle $\phi = 90^\circ$ while the wrist is executing the specified motion. Since the platform motion is often considerably slower than the arm movement, it is preferable *not* to move the platform continuously. To this end, instead of tracking the constraint $\phi = 90^\circ$ accurately, we can impose the inequality constraint

$$90^\circ - \delta \leq \phi \leq 90^\circ + \delta \quad (66)$$

where δ is a user-specified tolerance or margin. When the elbow angle ϕ is within the allowable bounds, the task weighting factor for ϕ is set to zero, and in this case base mobility will not be activated [unless the target wrist position is otherwise unattainable]. When ϕ is outside these bounds, i.e. $\phi > 90^\circ + \delta$ (arm over-stretched) or $\phi < 90^\circ - \delta$ (arm under-stretched), the task weighting for ϕ changes smoothly to one as shown in Figure 10 and the platform is moved automatically to restore the optimal configuration $\phi = 90^\circ$, without perturbing the wrist position. Thus the automatic motion of the base platform prevents undesirable over-stretched or under-stretched arm configurations, while enabling the wrist to reach positions in the workspace that would otherwise be unattainable.

Now let (x, y, z) represent the coordinates of the wrist and θ_5 be the x -coordinate of the base. The shoulder-wrist distance *SW* is given by

$$, \text{S11'} \quad r^2 = 4 \sin^2 \phi / 2z(x - \theta_5)^2 + y^2 + (z - h)^2 \quad (67)$$

For a given wrist position W , the elbow angle ϕ is determined *solely* by the base location θ_5 . To attain a desired elbow angle $\hat{\phi}$, the required base location is found from (67) as

$$\hat{\theta}_5 = x \pm w \quad (68)$$

where $w^2 = 4 \sin^2 \hat{\phi} / 2 - y^2 - (z - h)^2$. Equation (68) gives two solutions for the platform position $\hat{\theta}_5$, given the desired elbow angle $\hat{\phi}$. These solutions are symmetrical about the line perpendicular from W onto the x-axis. Because of the slow communication rate with the platform control unit, the arm-plus-platform control system is not implemented as an integrated 5 DOF system. Instead, a “4 + 1” DOF approach is adopted whereby motion commands for the platform position θ_5 are computed based on the arm configuration $\{\theta_1 \dots \theta_4\}$ using a stand-alone software, and are communicated through a serial port to the platform control unit for execution.

We shall now present the experimental results on real-time control of the mobile manipulator system. The purpose of the experiment is to demonstrate how base mobility can be used to appropriately move the arm in order to reach a target wrist position. In this experiment, the user has specified the task weightings W_t of 1 and feedback gains K of 1 for the wrist and arm angle control tasks, joint velocity weightings W_v of 0.005, and elbow angle margin $\delta = 30^\circ$. Starting from the initial wrist position of $x = -3.075m$, $y = -0.624m$, and $z = 1.200m$, and the initial arm angle $\psi = 45^\circ$, the wrist is commanded to move to the final position of $x = -3.925m$, $y = -0.624m$, and $z = 0.600m$ in 35 seconds while ψ remains constant. Note that the target wrist position is beyond the reach of the arm if base mobility is *not* activated. The elbow angle control is selected as the fifth task. Figure 11 shows the experimental results for the system. The plot shows that when the elbow angle exceeds 120° , the platform starts to move and brings the elbow angle back to approximately 90° . Notice that since the wrist velocity is greater than the base velocity, the elbow angle exceeds the user-specified range $60^\circ \leq \phi \leq 120^\circ$ momentarily until the base mobility has sufficient time to compensate for the wrist motion. Thus, the base mobility of the arm is used effectively to prevent the arm from reaching its workspace boundary.

5 Conclusions

Coordination of base mobility and arm manipulation in a mobile robot system is essential for successful execution of tasks. Using the configuration control formalism, a simple online approach is proposed in which the mobility and manipulation degrees-of-freedom both contribute to the end-effector task and the user-specified redundancy resolution goal, while satisfying the non-holonomic last constraint (if applicable). This formulation puts mobility and manipulation on the same footing, and treats them equally within a common framework.

The key advantages of the present approach over the previous schemes are its flexibility, simplicity, and computational efficiency. The ability to change the task specifications and the task weighting factors *on-line* based on the user requirements provides a flexible framework for mobile robot control. Furthermore, in contrast to some of the previous approaches which are suitable for off-line motion planning, the simplicity of the present approach leads to computational efficiency which is essential for on-line control in real-time implementations.

6 Acknowledgment

The research described in this paper was carried out at the Jet Propulsion Laboratory, California Institute of Technology, under contract with the National Aeronautics and Space Administration.

References

- [1] W. F. Carriker, P. K. Khosla, and J. J. Krogh: "Path planning for mobile manipulators for multiple task execution," IEEE Trans. on Robotics and Automation, Vol. 7, No.3, pp. 403-408, June 1991.
- [2] W. F. Carriker, J. K. Khosla, and J. J. Krogh: "The use of simulated annealing to solve the mobile manipulator path planning problem," Proc. IEEE Intern. Conf. on Robotics and Automation, pp. 204-209, May 1990.
- [3] F. G. Pin and J. C. Culoli: "Optimal positioning of redundant manipulator - platform systems for maximum task efficiency," Proc. Intern. Symposium on Robotics and Manufacturing, pp. 489-495, July IWO.
- [4] F. G. Pin and J. C. Culoli: "Multi-criteria position and configuration optimization for redundant platform/manipulator systems," Proc. IEEE Workshop on Intelligent Robots and Systems, pp. 103-107, July 1990.
- [5] N. A. M. Hootsmans and S. Dubowsky: "Large motion control of mobile manipulators including vehicle suspension characteristics," Proc. IEEE Intern. Conf. on Robotics and Automation, pp. 2336-2341, April 1991.
- [6] J. J. Seraji: "An on-line approach to coordinated mobility and manipulation," Proc. IEEE Intern. Conf. on Robotics and Automation, Vol. 1, pp. 28-35, Atlanta, May 1993.
- [7] J. Barraquand and J. C. Latombe: "On nonholonomic mobile robots and optimal maneuvering," Proc. 4th IEEE Intern. Symposium on Intelligent Control, pp. 340-347, Albany, September 1989.

- [8] Y. Yamamoto and X. Yun: "Coordinating locomotion and manipulation of a mobile manipulator," Proc. 31st IEEE Conf. on Decision and Control, pp. 2643-2648, Tucson, December 1992,
- [9] Y. Yamamoto and X. Yun: "Control of mobile manipulators following a moving surface," Proc. IEEE Intern. Conf. on Robotics and Automation, Vol. 3, pp. I-(i), Atlanta, May 1993.
- [10]** C. C. Wang, N. Sarkar, and V. Kumar: "Rate kinematics of mobile manipulators," Proc. 22nd Biennial ASME Mechanisms Conf., pp. 2,25-232, Scottsdale, September 1992.
- [11] C. C. Wang and V. Kumar: "Velocity control of mobile manipulators," Proc. IEEE Intern. Conf. on Robotics and Automation, Vol. 2, pp. 713-718, Atlanta, May 1993.
- [12] L. Liu and F. L. Lewis: "Control of mobile robot with onboard manipulator," Proc. Intern. Symposium on Robotics and Manufacturing, Vol. 4, pp. 539-546, Santa Fe, November 1992.
- [13] S. Jagannathan, H. Liu, and L. Liu: "Modeling, control and obstacle avoidance of a mobile robot with an onboard manipulator," Proc. IEEE Intern. Symp. on Intelligent Control, Chicago, August 1993.
- [14] H. Seraji: "Configuration control of redundant manipulators: Theory and implementation," IEEE Trans. on Robotics and Automation, Vol. 5, No. 4, pp. 472-490, 1989.
- [15] H. Seraji and R. Colbaugh: "Improved configuration control for redundant robots," Journal of Robotic Systems, Vol. 7, No. 6, pp. 897-928, 1990.
- [16] J. J. Craig: *Robotics - Mechanics and Control*, Addison Wesley Publishing Company, New York, 1986.
- [17] D.E. Whitney: "The mathematics of coordinated control of prosthetic arms and manipulators," ASME Journ. Dyn. Syst., Meas. and Control, Vol. 94, No. 14, pp. 303-309 1972.
- [18] T. Yoshikawa: "Manipulability and redundancy control of robotic mechanisms," Proc. IEEE Conf. on Robotics and Automation, pp. 1004-1009, March 1985.
- [19] L. Kreutz, M. Long, and H. Seraji: "Kinematic analysis of 7 DOF manipulators," Intern. Journal of Robotics Research, No. 5, pp. 469-481, 1992.

7 Appendix

In this Appendix, we discuss the effect of base mobility on the end-effector manipulability index.

Consider the end-effector manipulability index given by equation (35) as

$$\mu_e = \{\det[J_e J_e^T]\}^{1/2} = \{\det[J_a J_a^T + J_b J_b^T]\}^{1/2} \quad (69)$$

When the arm is in a non-singular configuration, J_a is of full rank and $J_a J_a^T$ is a positive-definite matrix. Hence, equation (69) can be written as

$$\det[J_e J_e^T] = \det[J_a J_a^T] \cdot \det[I + (J_a J_a^T)^{-1} J_b J_b^T] \quad (70)$$

Let us now express $J_a J_a^T$ and $J_b J_b^T$ as the products

$$J_a J_a^T = S^T S ; \quad J_b J_b^T = S^T C S$$

where S is a non-singular matrix and $C = S^{-T} (J_b J_b^T) S^{-1}$. Then we obtain

$$\begin{aligned} \det[I + (J_a J_a^T)^{-1} (J_b J_b^T)] &= \det[I + S^{-1} C S] \\ &= \det[I + C] \\ &= \prod_{i=1}^m (1 + \sigma_i) \end{aligned} \quad (71)$$

where $\sigma_i (\geq 0)$ are the eigenvalues of C . Thus from equations (69) and (71), we have

$$\mu_e = \mu_a [\prod (1 + \sigma_i)]^{1/2} = \mu_a + 0 \quad (72)$$

while σ is positive and hence $\mu_e > \mu_a$.

When the arm is in a singular configuration, J_a is rank-deficient and hence $J_a J_a^T$ is a positive semi-definite matrix. In this case, if the last is in a non-singular configuration, i.e., J_b is of full rank, the above analysis can be repeated with J_a replaced by J_b to show that $\mu_e > \mu_a$. However, if the base is also in a singular configuration, $J_b J_b^T$ is positive semi-definite and the end-effector manipulability index μ_e may be zero, that is, $\mu_e \geq \mu_a (= 0)$.

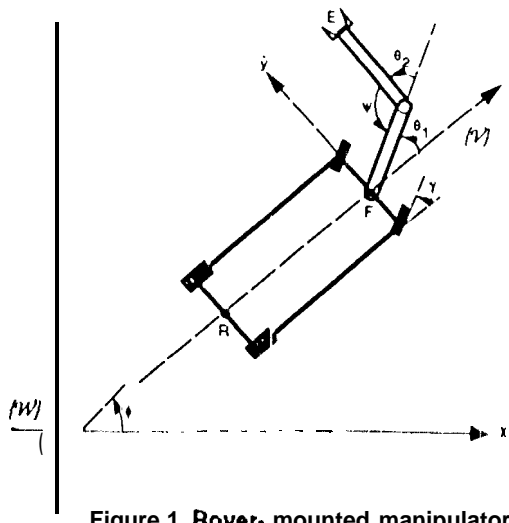


Figure 1. Rover-mounted manipulator

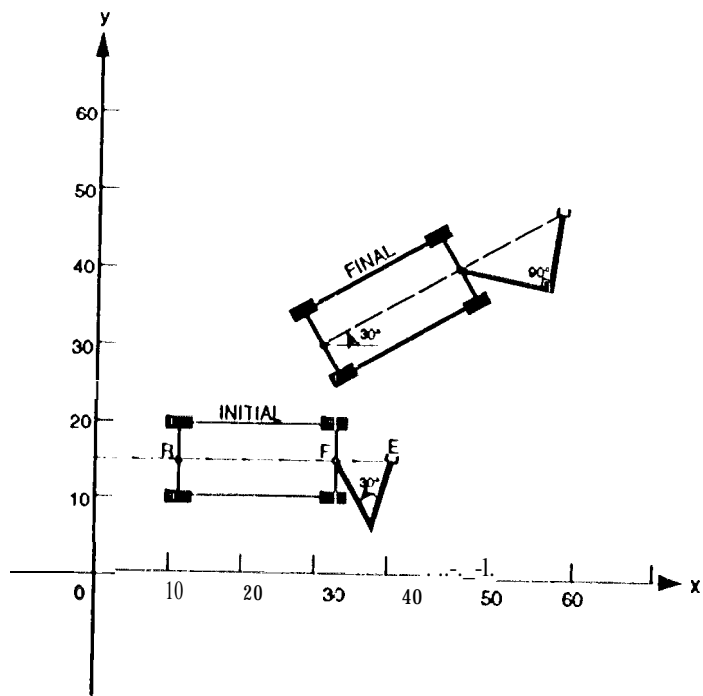


Figure 2. Initial and final configurations in the simulation study (not drawn to scale)

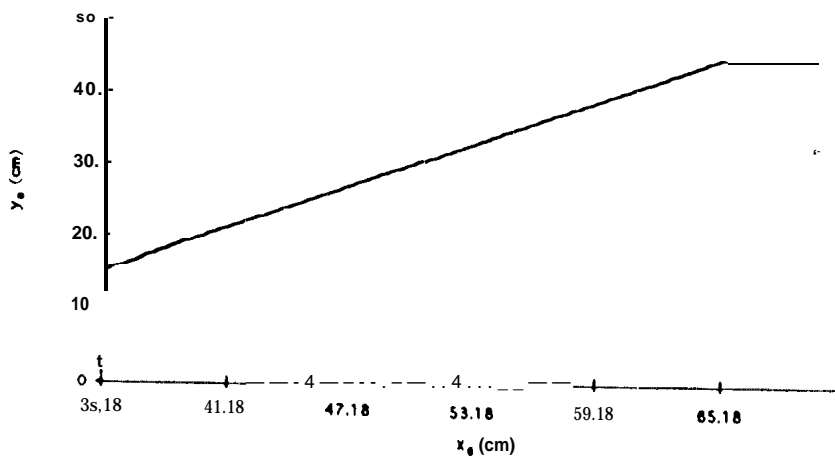


Figure 3a. Motion trajectory of the end-effector E

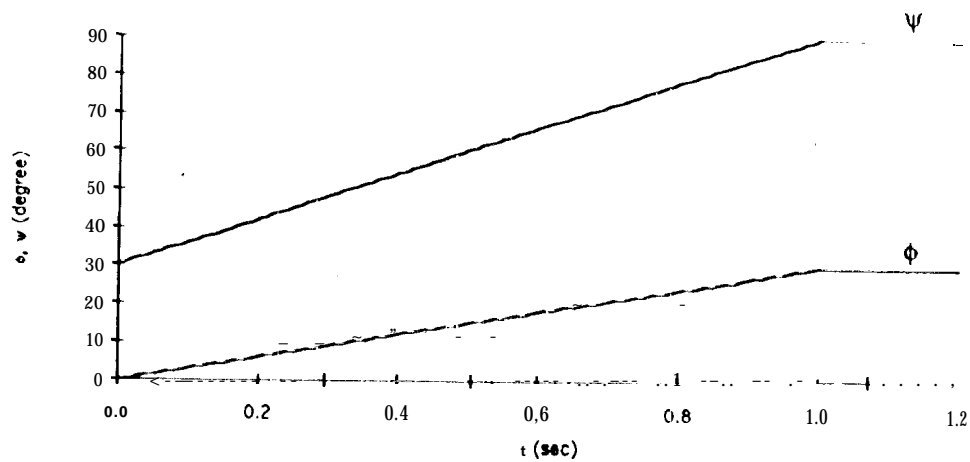


Figure 3b. Variations of the rover orientation ϕ and elbow angle ψ

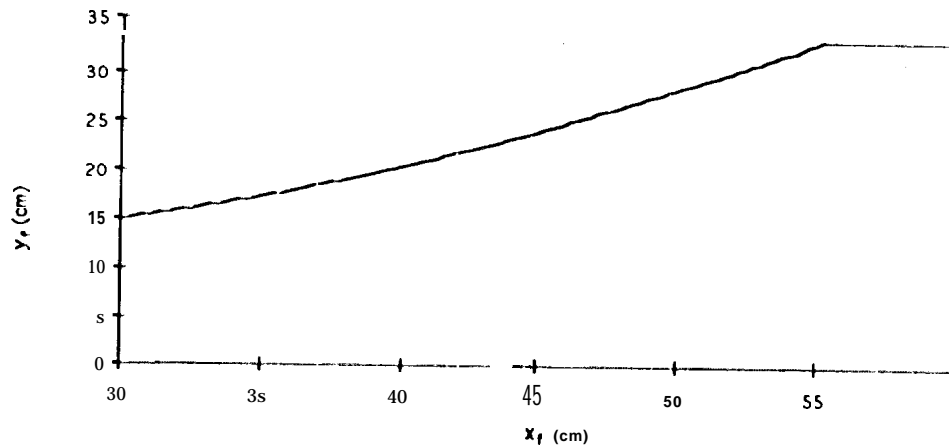


Figure 3c. Motion trajectory of the rover front midpoint F

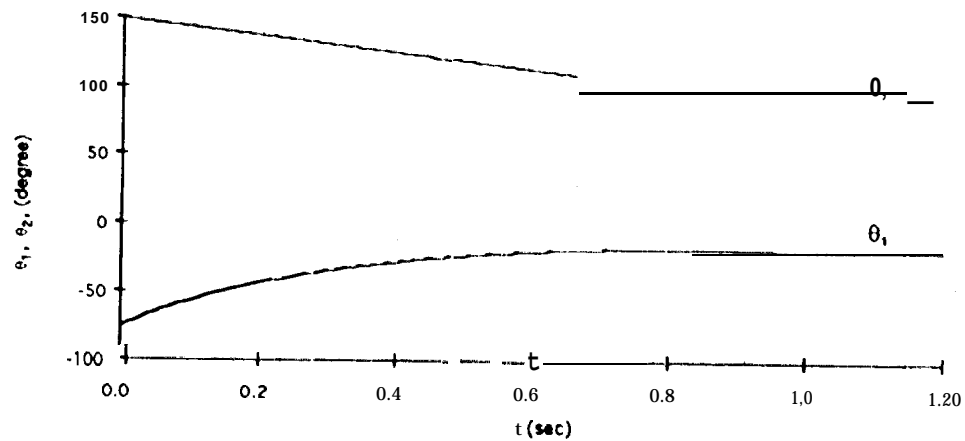


Figure 3d. Variations of the arm joint angles θ_1 and θ_2

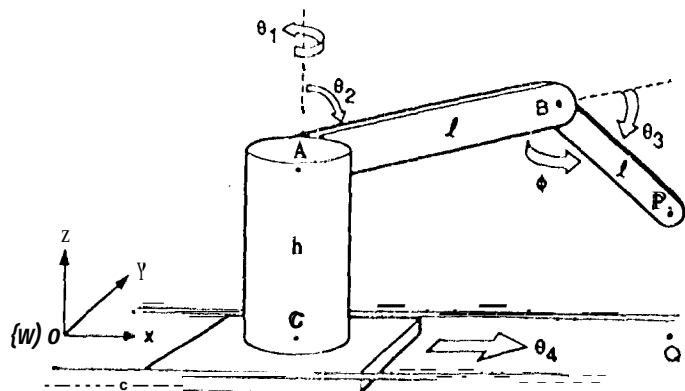


Figure 4. A PUMA-like robot mounted on a track

	t (sec)	x (cm)	y (cm)	z (cm)	ϕ (deg)	θ_1 (deg)	θ_2 (deg)	θ_3 (deg)	θ_4 (cm)
a = 0	2.0	386.6	50.0	225.0	90.0	49.1	72.9	-90.0	343.3
$\alpha = 1$	2.0	384.2	48.2	220.5	92.1	37.6	77.1	-87.8	321.7
a = 10	2.0	341.8	37.3	193.2	108.7	16.3	90.7	-71.3	214.0

Table 1. Effect of α on steady-state performance with $\beta = 1$

	t (See)	x (cm)	y (cm)	z (cm)	ϕ (deg)	θ_1 (deg)	e_2 (deg)	θ_3 (deg)	θ_4 (cm)
$\alpha = 0$	2.0	386.6	50.0	225.0	90.0	49.1	72.9	-90.0	343.3
$\beta = 1$									
$a = 1$	2.0	383.9	48.2	220.5	94.3	35.2	77.6	-85.7	315.5
$\beta = 1/2$									
$\alpha = 10$	2.0	351.3	41.1	202.7	152.2	14.4	72.0	-27.8	191.8
$\beta = 1/11$									

Table 2. Effect of a and β on steady-state performance

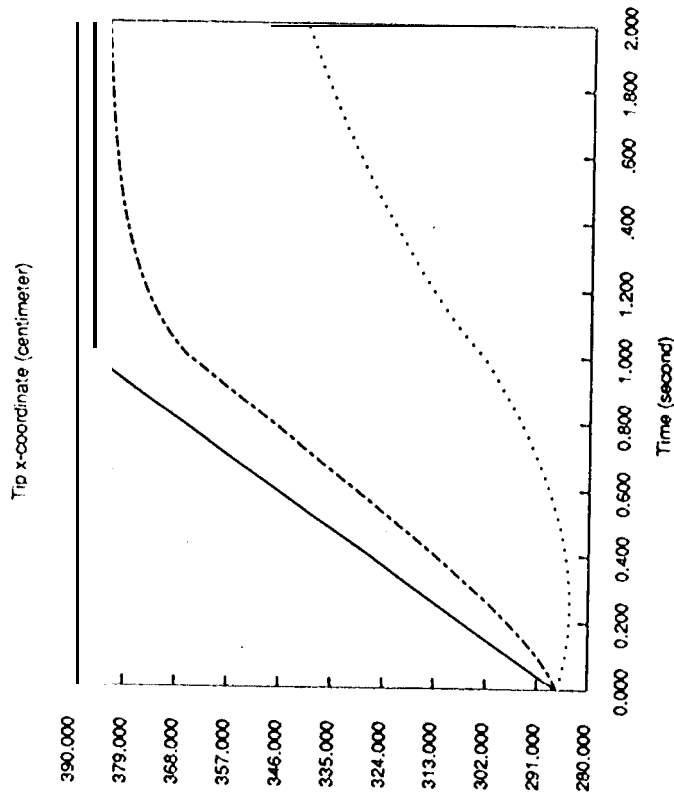


Figure 5a. Response of the tip x-coordinate
($\alpha = 0$ solid, $\alpha = 1$ dot-dashed, $\alpha = 10$ dotted)

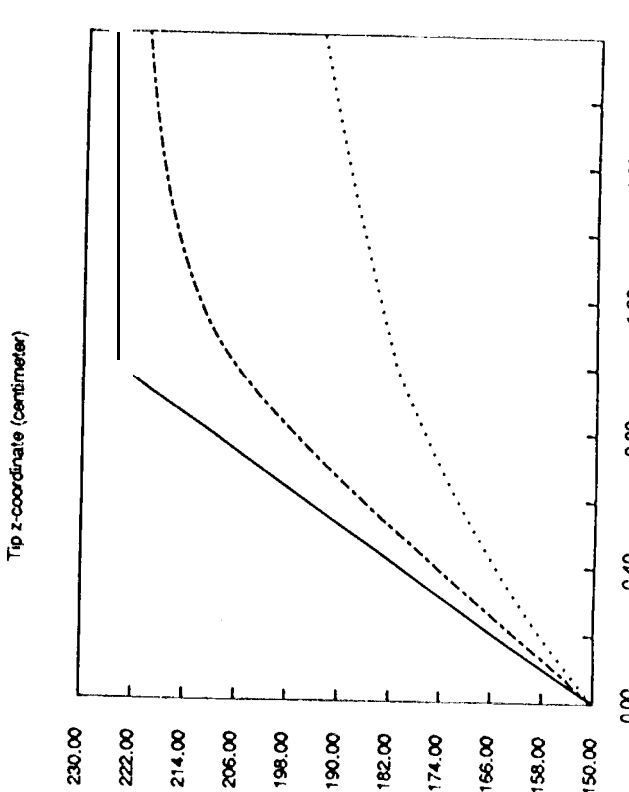


Figure 5c. Response of the tip z-coordinate

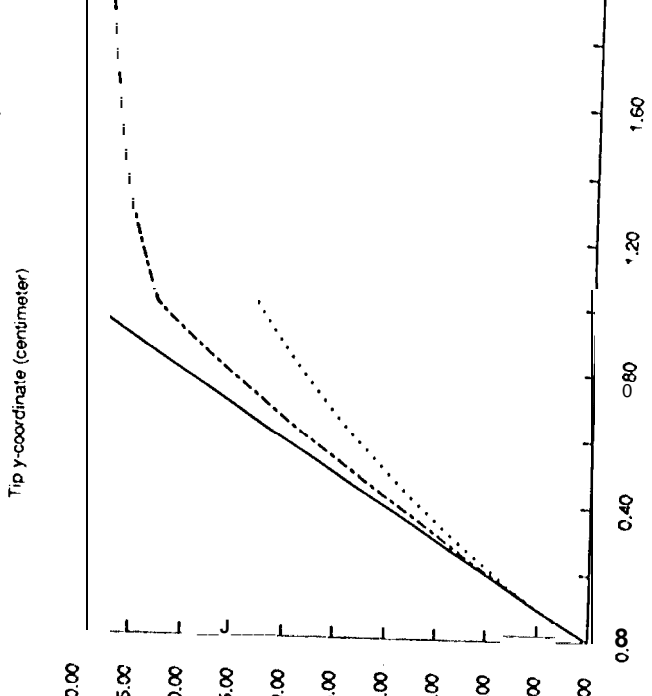


Figure 5b. Response of the tip y-coordinate
($\alpha = 0$ solid, $\alpha = 1$ dot-dashed, $\alpha = 10$ dotted)

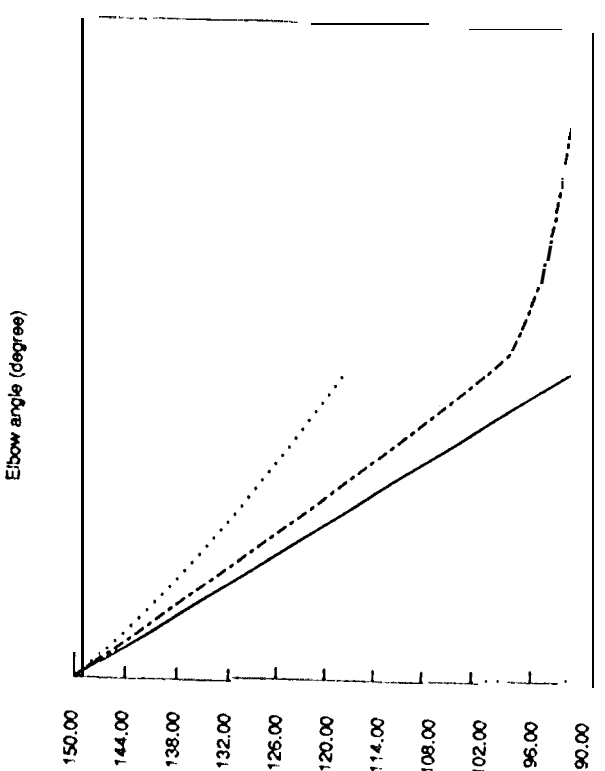


Figure 5d. Response of the elbow angle

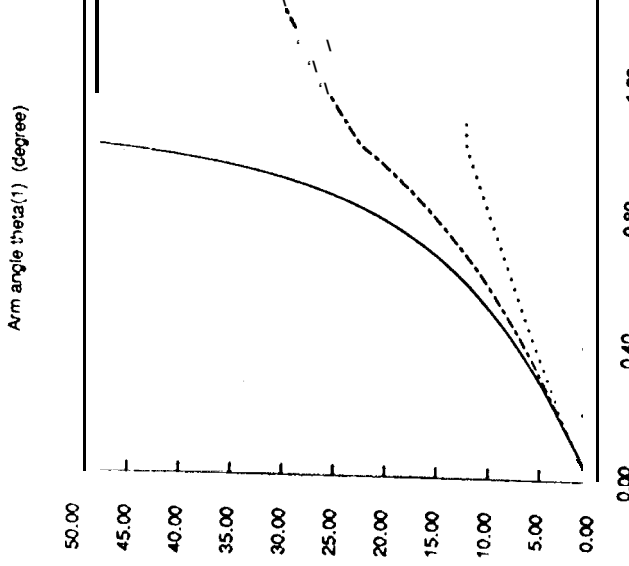


Figure 5e. Variation of the arm angle θ_1 , ($\alpha = 0$ solid, $\alpha = 1$ dot-dashed, $\alpha = 10$ dotted)

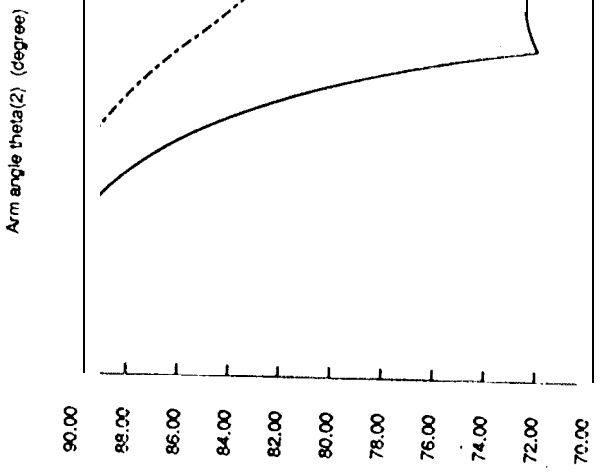


Figure 5f. Variation of the arm angle θ_2 , ($\alpha = 0$ solid, $\alpha = 1$ dot-dashed, $\alpha = 10$ dotted)

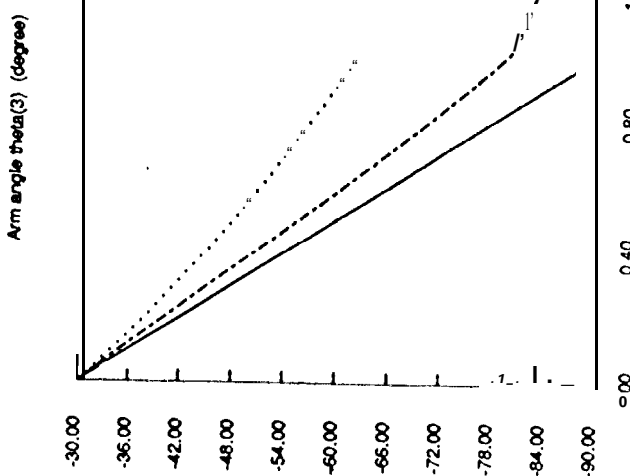


Figure 5g. Variation of the arm angle θ_3 , ($\alpha = 0$ solid, $\alpha = 1$ dot-dashed, $\alpha = 10$ dotted)

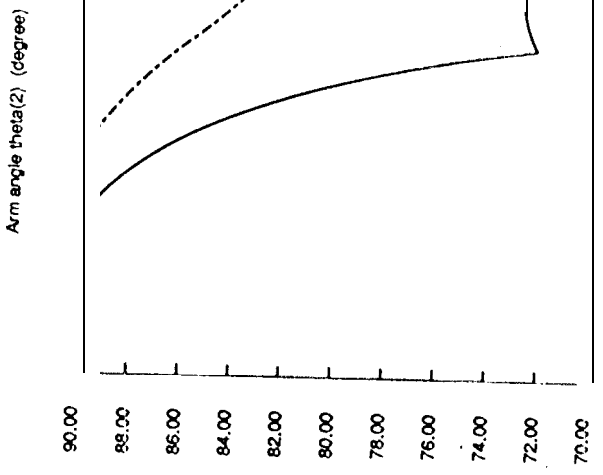


Figure 5h. Variation of the base position, ($\alpha = 0$ solid, $\alpha = 1$ dot-dashed, $\alpha = 10$ dotted)

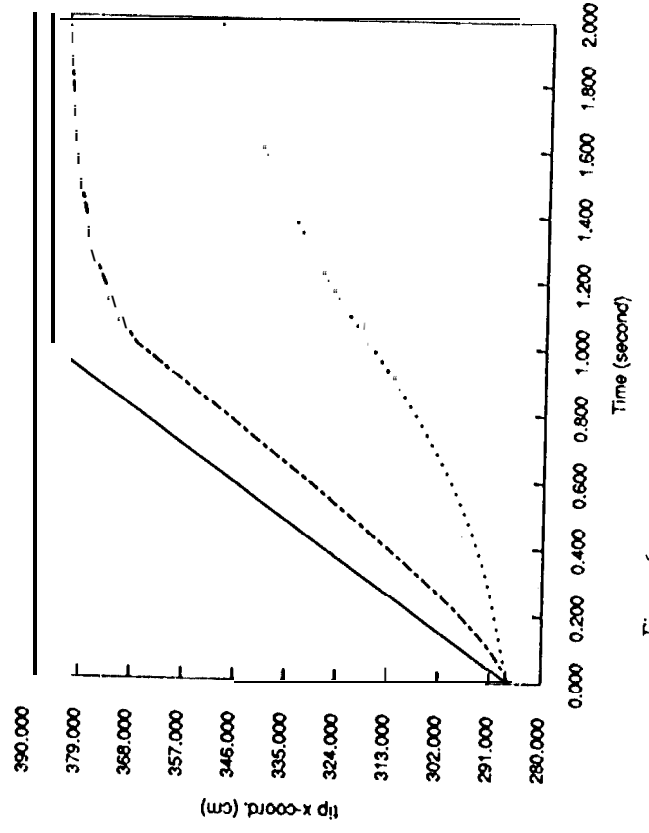


Figure 6a. Response of the tip x-coordinate
($\alpha = 0$ solid, $\alpha = 1$ dot-dashed, $\alpha = 10$ dotted).

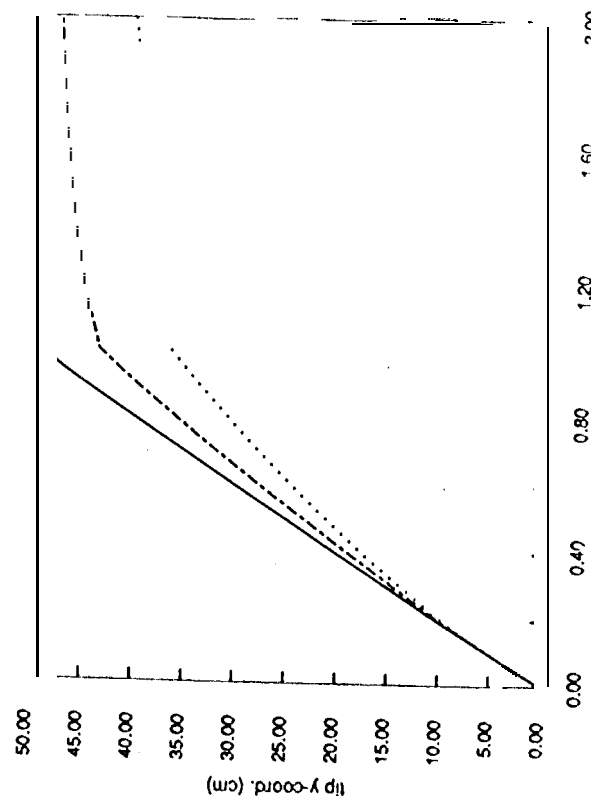


Figure 6b. Response of the tip y-coordinate
($\alpha = 0$ solid, $\alpha = 1$ dot-dashed, $\alpha = 10$ dotted).

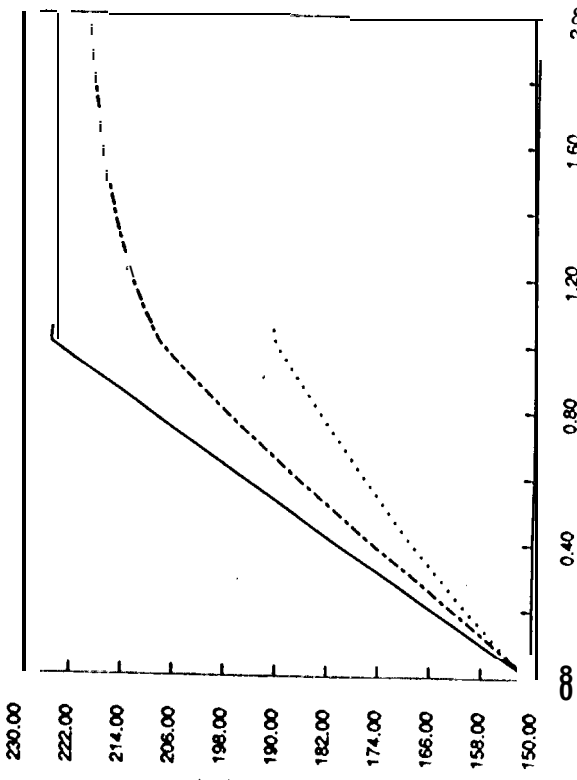


Figure 6c. Response of the tip z-coordinate
($\alpha = 0$ solid, $\alpha = 1$ dot-dashed, $\alpha = 10$ dotted).

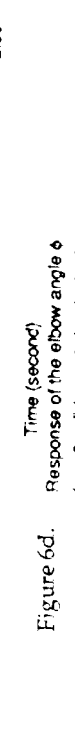


Figure 6d. Response of the elbow angle ϕ
($\alpha = 0$ solid, $\alpha = 1$ dot-dashed, $\alpha = 10$ dotted).

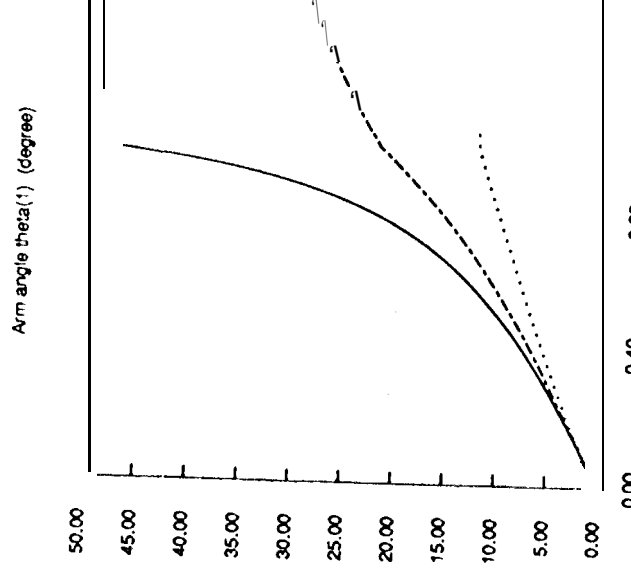


Figure 6e. Variation of the arm angle θ_1
 $(\alpha = 0 \text{ solid}, \alpha = 1 \text{ dot-dashed}, \alpha = 10 \text{ dotted})$

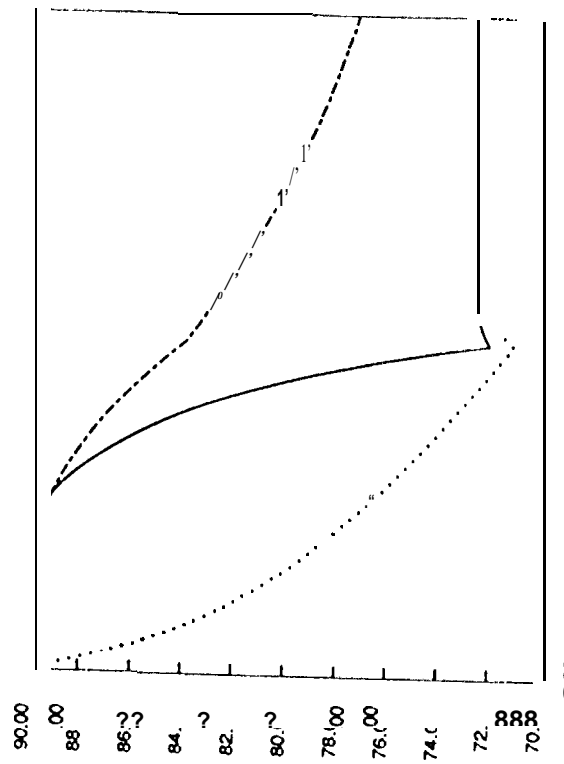


Figure 6f. Variation of the arm angle θ_2
 $(\alpha = 0 \text{ solid}, \alpha = 1 \text{ dot-dashed}, \alpha = 10 \text{ dotted})$

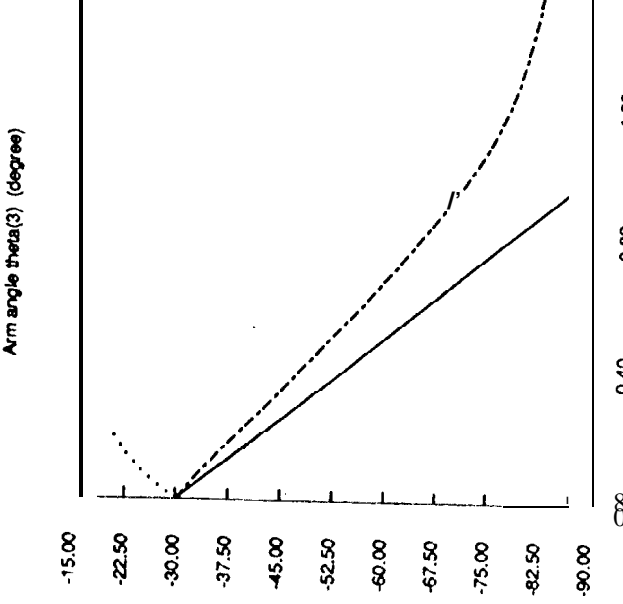


Figure 6g. Variation of the arm angle θ_3
 $(\alpha = 0 \text{ solid}, \alpha = 1 \text{ dot-dashed}, \alpha = 10 \text{ dotted})$

Arm angle theta(2) (degree)

Time (second)

Arm angle theta(1) (degree)

Time (second)

Arm angle theta(3) (degree)

Time (second)

Time (second)

Time (second)

Time (second)

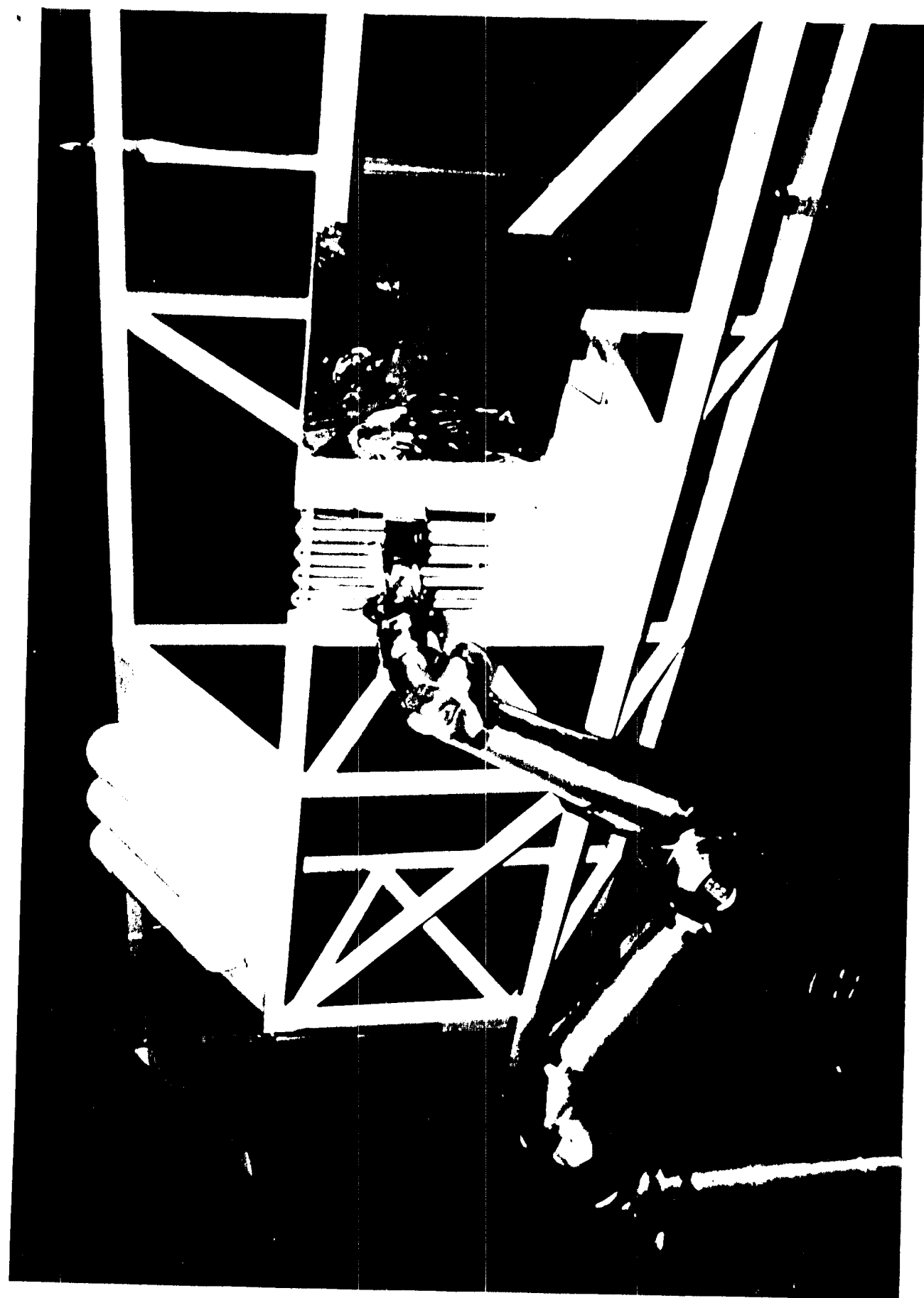


Figure 7: JPL Surface Inspection Laboratory

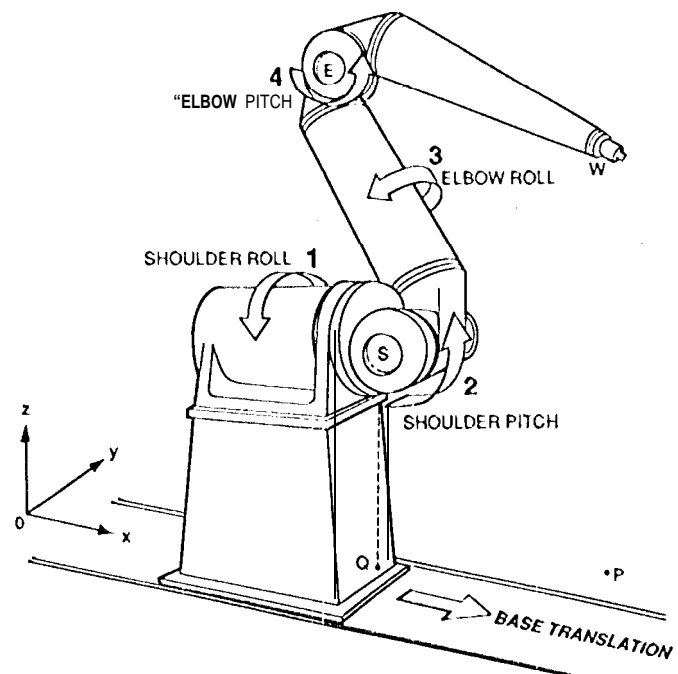


Figure 8. A Robotics Research arm mounted on a mobile platform

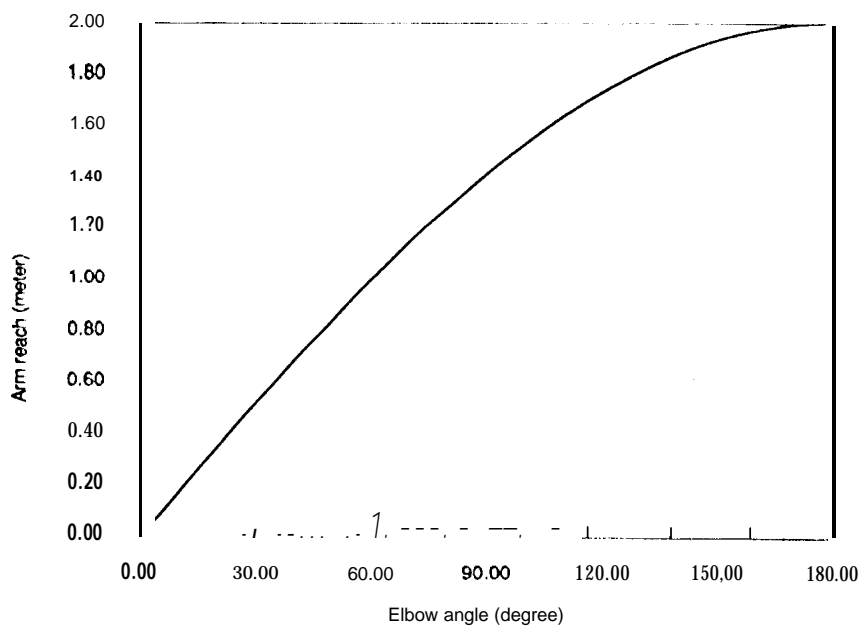


Figure 9. Variation of the arm reach, as a function of the elbow angle

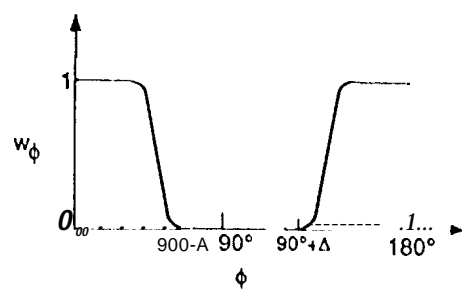


Figure 10. Variation of the task weighting factor as a function of the elbow angle

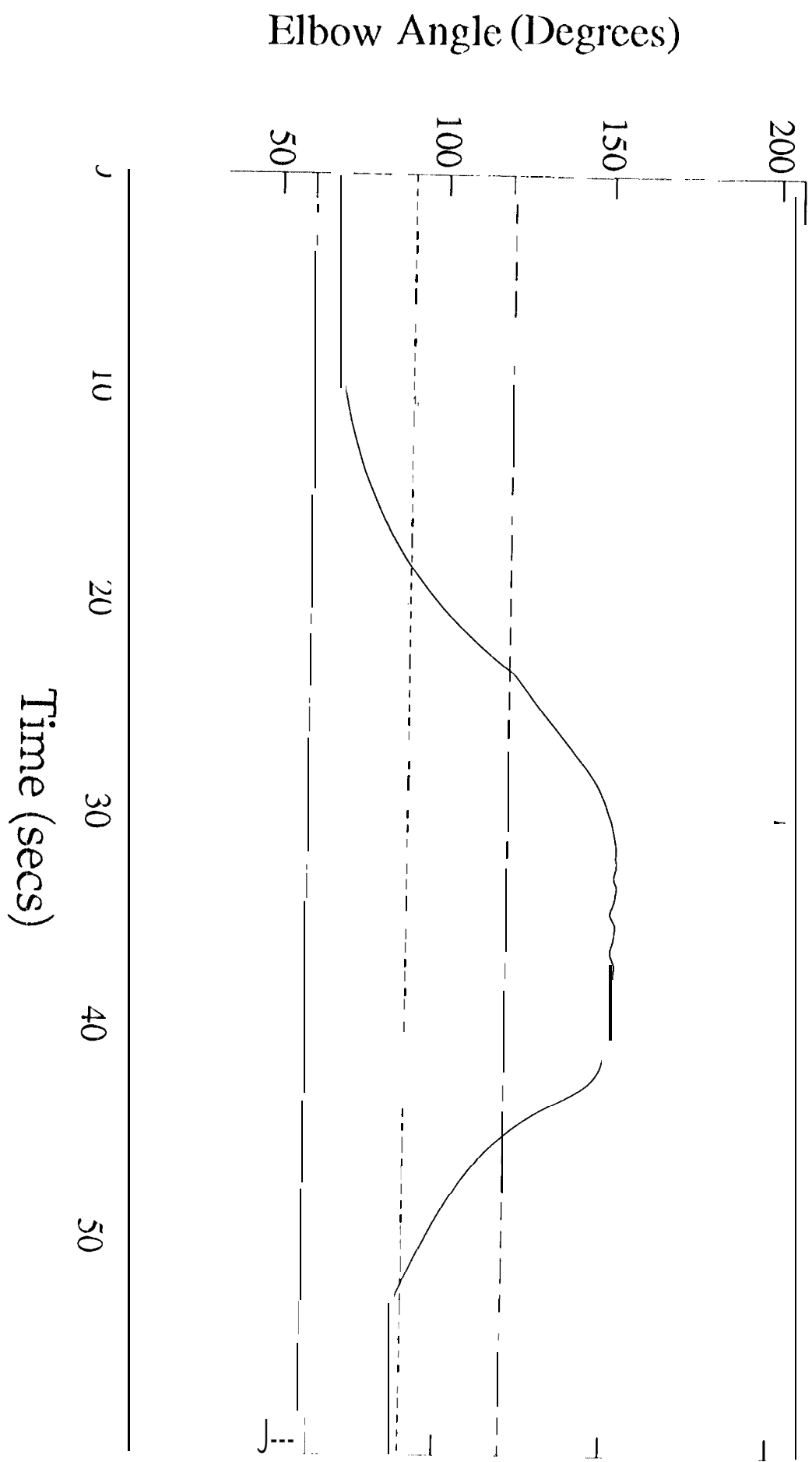


Figure 11. Experimental Data